

# THE REDSHIFT EVOLUTION OF THE METAGALACTIC IONIZING FLUX INFERRED FROM METAL LINE RATIOS IN THE LYMAN FOREST

ANTOINETTE SONGAILA<sup>1</sup>

Institute for Astronomy, University of Hawaii, 2680 Woodlawn Drive, Honolulu, HI 96822

Received 1998 February 9

## ABSTRACT

Metal line ratios in a sample of 13 quasar spectra obtained with the HIRES spectrograph on the Keck I Telescope have been analyzed to characterize the evolution of the metagalactic ionizing flux near a redshift of 3. The evolution of Si iv/C iv has been determined using three different techniques: using total column densities of absorption-line complexes, as in the approach of Songaila & Cowie, using the column densities of individual Voigt profile components within complexes, and using direct optical depth ratios. All three methods show that Si iv/C iv changes abruptly at  $z \sim 3$ , requiring a jump in value of about a factor of 3.4 and indicating a significant change in the ionizing spectrum that occurs rapidly between  $z = 2.9$  and  $z = 3$ , just above the redshift at which Reimers et al. detected patchy He ii Ly $\alpha$  absorption. At lower redshifts, the ionization balance is consistent with a pure power-law ionizing spectrum, but at higher redshifts the spectrum must be very soft, with a large break at the He<sup>+</sup> edge. An optical depth ratio technique is used to measure the abundances of ions whose transitions lie within the forest, and C iii, Si iii, and O vi are detected in this way. The presence of a significant amount of O vi at  $z > 3$  suggests either a considerable volume of He iii bubbles embedded in the more general region in which the ionizing flux is heavily broken or the addition of collisional ionization to the simple photoionization models.

*Key words:* early universe — galaxies: formation — intergalactic medium — quasars: absorption lines

## 1. INTRODUCTION

Whereas we know from the absence of any significant Gunn-Peterson effect even in the highest redshift quasars that hydrogen reionization of the intergalactic gas must have taken place at  $z > 5$ , we have much less information about the period at which the bulk of singly ionized helium converted to doubly ionized helium. Since late He<sup>+</sup> ionization may significantly change the temperature of the intergalactic gas, it is critical to understand this heating if we are to correctly model the growth of structure in the intergalactic medium (IGM) and determine the mapping of the baryon density to observable quantities such as observations of the neutral hydrogen Ly $\alpha$  forest and the He<sup>+</sup> Ly $\alpha$  opacity. Phenomenological modeling of this event depends critically on the softness of the composite spectrum of the ionizing sources (e.g., Miralda-Escudé & Rees 1993; Madau & Meiksin 1994), amplified by the subsequent radiative transfer, and such models cannot be considered reliable in predicting the high-energy ( $E > 54$  eV) metagalactic ionizing spectrum above the He<sup>+</sup> ionization edge, which determines the fraction of singly ionized helium.

Our most direct information on the He<sup>+</sup> opacity is through observations of quasars whose spectra extend to the He<sup>+</sup> Ly $\alpha$  wavelength. Despite the extreme difficulty of these measurements, successful observations of the He<sup>+</sup> Ly $\alpha$  absorption have been made toward  $z > 2.8$  quasars with the *Hubble Space Telescope* (HST) (Jakobsen et al. 1994; Hogan, Anderson, & Rugers 1997; Reimers et al. 1997) and of the  $z = 2.72$  quasar HS 1700+6416 with the Hopkins Ultraviolet Telescope (Davidsen, Kriss, & Zheng 1996; Zheng, Davidsen, & Kriss 1998). The He<sup>+</sup> Ly $\alpha$

opacity shows a marked decrease from a value of  $\tau = 3.2^{+1.1}_{-1.1}$  in Q0302–003 at  $z = 3.29$  to  $\tau = 1.0 \pm 0.07$  in HS 1700+6416. More remarkably, the Reimers et al. observation of the intermediate-redshift quasar HE 2347–4342 at  $z = 2.89$  shows both “troughs” and “voids” in the He ii Ly $\alpha$  observations, suggesting that at  $z \sim 2.8$  we are seeing fully ionized He ii bubbles interspersed among as yet un-ionized He<sup>+</sup> regions and that it is at this point that the porosity of He iii regions is approaching unity and the universe is becoming He ii-transparent.

The recent discovery that the bulk of Ly $\alpha$  forest absorption with  $N(\text{H I}) > 3 \times 10^{14} \text{ cm}^{-2}$  contains associated metals (Songaila & Cowie 1996, hereafter SC) provides us with an alternative approach to the problem since ionization balance in these forest metals is a diagnostic of the shape of the metagalactic flux in the neighborhood of the He<sup>+</sup> edge. As was first noted in Songaila et al. (1995), the value of Si iv/C iv in high-ionization systems is critically dependent on the He<sup>+</sup> ionization edge break strength. This has subsequently been investigated in more detail by SC, Savaglio et al. (1997), and Giroux & Shull (1997), among others. As will be discussed below, the bulk of the forest metal line systems at the currently observed redshifts ( $z \sim 2\text{--}4$ ) are high ionization ( $\text{C II/C IV} \ll 0.1$ ), and so, unless there is a strong break at the edge, they will have Si iv/C iv  $\ll 0.1$  even for the higher Si/C abundances characteristic of low-metallicity systems. Therefore, once the He<sup>+</sup> is fully ionized and the IGM becomes relatively transparent to the integrated quasar spectrum (e.g., in the metagalactic spectrum of Haardt & Madau 1996), the observed Si iv/C iv values should fall in this low range. SC and Savaglio et al. (1997) have shown that, whereas this is generally true at  $z < 3$ , much higher Si iv/C iv values are regularly seen at  $z > 3$ , suggesting a significant change above this redshift, which would be consistent with the interpretation of the Reimers et al. (1997) observations as showing the redshift at

<sup>1</sup> Visiting Astronomer at the W. M. Keck Observatory, jointly operated by the California Institute of Technology and the University of California.

which He III bubbles begin to overlap. Boksenberg (1998) has recently questioned this result, based on an analysis of the redshift evolution of the ion ratios in the separate Voigt profile components in complex systems rather than in the integrated column densities of the complexes. However, his analysis is based on rather a small sample of systems without clear selection criteria. In this paper, I shall use the largest sample to date to demonstrate unambiguously that, irrespective of the method of analysis, there is indeed a rapid jump in the value of Si IV/C IV at a redshift just below 3 and that the ionization stages in the metals are consistent with this being, for most systems, the point at which they change from being ionized by a metagalactic spectrum, that is, at  $z > 3$ , heavily broken above 54 eV, to one that is only mildly broken at the lower redshifts.

The sample and the data reduction are described in § 2; the reader who is primarily interested in the results can safely skip this section. The evolution of the C II/C IV and Si IV/C IV values with redshift is described in § 3, in which I show that the presence of a jump in Si IV/C IV values at  $z$  just under 3 is highly significant and does not depend on the method of analysis, whether by total column densities of complex, by the column densities of individual Voigt components, or by directly analyzing the distribution of optical depth ratios. In § 4, I consider the overall ionization balance including intermediate ionization stages such as C III and Si III and high ions such as N V and O VI, using, for those lines that lie primarily within the forest, the optical depth distributions of the ensembles of such lines, which provides a new and robust technique for determining their properties. The overall ionization balance is broadly consistent with unbroken power-law photoionization at  $z < 3$ ; however, the observation of significant amounts of O VI at  $z > 3$  requires either the presence of a considerable volume of He III bubbles permeating regions where the ionizing flux is heavily broken or the addition of collisional ionization to the simple photoionization models. Finally, the conclusions are briefly summarized in § 5.

## 2. DATA

The sample was drawn from observations of 13 quasars with complete or near-complete coverage between the quasars' Ly $\alpha$  and C IV emission lines. All observations (summarized in Table 1) were made with the HIRES

spectrograph on the 10 m Keck I Telescope using a  $1''.14 \times 7''$  slit, which gives a resolution of  $R = 37,000$ , and with total exposure times from 3.3 hr to just over 10 hr. The approximate signal-to-noise ratio (S/N) per resolution element for each quasar at wavelengths between Ly $\alpha$  and C IV emission is summarized in Table 1 and ranges from 60 (Q0256–000) to 330 (Q1422+231).

Individual exposures were generally set to 40 minutes (providing a reasonable compromise between minimizing cosmic-ray hits and read noise effects) and with the 2048 Tektronix CCD read out with a binning of 2 in the spatial direction and 1 in the spectral direction, resulting in a spatial pixel of  $0''.38$  and  $\Delta\lambda/\lambda = 7.3 \times 10^{-6}$ ; this substantially oversamples the resolution element. For the higher redshift quasars several settings of the HIRES cross-disperser were used to provide the full wavelength coverage. All but three of the quasars have full coverage of the wavelength region of interest (Table 1, col. [5]) and the remaining three have small interorder gaps. In general, the spectra extend from approximately 3800 Å, below which the HIRES sensitivity begins to fall rapidly, up to the wavelength of the quasar's C IV emission. A white dwarf star and the ThAr calibration lamp were also observed either immediately before or immediately after each sequence of exposures on a quasar.

A relatively straightforward extraction technique was used since optimization does not provide substantial gains for these spatially undersampled and signal-dominated spectra. Starting from approximate order and wavelength solutions, the position and shape of each order on the CCD were determined from the observations of the white dwarf. Only orders lying fully on the CCD were extracted. A small number of known bad points and columns were cleaned by interpolation, and a number of regions, such as the central blemish on the chip, were flagged as unusable. The first-pass cosmic-ray rejection was made by forming a residual image with a five-point two-dimensional median subtracted and then subtracting an 11-point row-by-row median. Any points in this differenced image that exceeded expected values by more than  $4\sigma$  were interpolated from neighboring points along the column (spatial) direction.

The spectral image was distorted by bilinear interpolation to make the echelle order parallel to the rows. The sky was then determined from the median of pixels on the

TABLE 1  
OBSERVATIONS

Quasar (1)	Magnitude (2)	Exposure (hr) (3)	S/N (4)	Complete? (5)	$z_{\text{low}}$ (Si IV) (6)	$z_{\text{low}}$ (C II) (7)	$z_{\text{high}}$ (8)
0014+813 .....	16.5	7.65	120	Yes	2.81	3.00	3.31
0256–000 .....	18.2	5.33	60	Yes	2.78	2.97	3.28
0302–003 .....	17.8	10.67	90	Yes	2.72	2.91	3.21
0636+680 .....	16.5	6.08	130	Yes	2.62	2.80	3.10
0741+4741 .....	16.1	4.0	145	No	2.66	2.84	3.15
0956+122 .....	17.5	6.67	90	Yes	2.74	2.92	3.23
1159+123 .....	17.5	8.0	85	Yes	2.90	3.09	3.42
1422+231 .....	16.5	9.3	330	Yes	3.01	3.21	3.54
1623+269 .....	16.0	3.33	60	Yes	2.12	2.27	2.48
1700+6416 .....	16.1	8.33	260	Yes	2.27	2.43	2.68
2000–330 .....	19.0	4.67	60	Near	3.14	3.36	3.69
2126–158 .....	17.3	4.45	130	No	2.72	2.90	3.21
2347–4342 .....	16.3	6.67	130	Yes	2.37	2.54	2.82

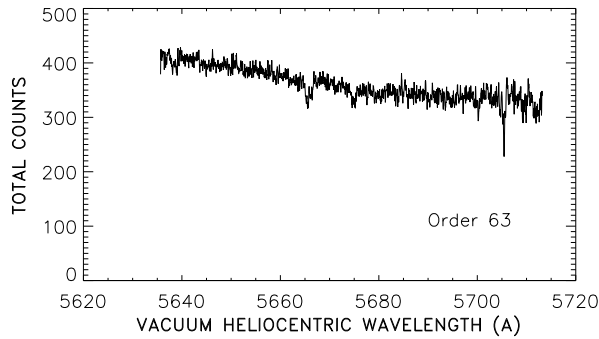


FIG. 1a

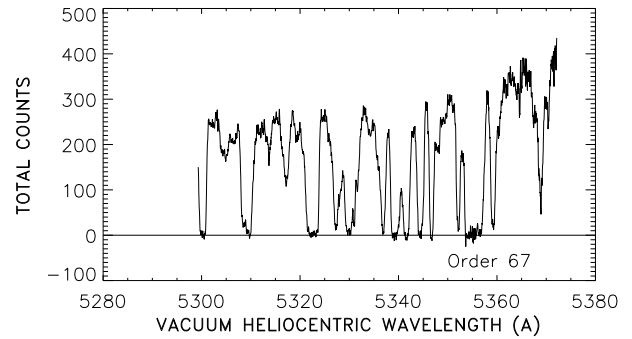


FIG. 1b

FIG. 1.—(a) Sample extraction of one of the orders longward of the  $\text{Ly}\alpha$  forest in the quasar Q1159+123. The total exposure is 2 hr, consisting of three 40 minute integrations. The spectrum is unsmoothed and oversamples the resolution element. (b) Order in the same spectrum as (a), but lying in the  $\text{Ly}\alpha$  forest. The precision of the sky subtraction may be assessed from the degree to which the bases of the saturated  $\text{Ly}\alpha$  lines approximate to zero.

same column lying between  $2''$  and  $3.5''$  on either side of the maximum signal and subtracted from the spectral image, and the spectrum was extracted in a  $\pm 1''$  window. The spectra for all the subexposures were then combined with an optimal S/N weighting, and any residual cosmic-ray structure was removed by identifying any strongly deviant (greater than  $5\sigma$ ) points in the individual spectrum and flagging and removing these from a second and final summation. The blaze function was determined from a normalized fifth-order polynomial fit to the white dwarf spectrum, iteratively repeated to exclude any absorption lines and divided into the spectrum. The wavelength and spectrum for each order were then individually stored.

The ThAr calibration spectrum was extracted in the same fashion as the object spectrum but without any sky subtraction step. For each order, each of the stronger unblended calibration lines was fitted with a Gaussian to determine its centroid, and a third-order polynomial fit was then applied to determine the wavelength solution. From 10 to 30 calibration lines were used for each order, and the rms residual was normally less than  $2 \times 10^{-3} \text{ \AA}$ , so that velocities should be accurate to better than  $0.1 \text{ km s}^{-1}$ . Finally, the wavelength scale was converted to vacuum heliocentric, which is used throughout this paper.

A typical extracted order longward of the forest is shown in Figure 1a, which shows order 63 from a 2 hr exposure of Q1159+123 obtained as three 40 minute exposures in 1997 April. The absorption lines in the center of the order are a C iv doublet, and the rise in flux to shorter wavelengths

reflects the onset of the quasar's  $\text{Ly}\alpha$  and N v emission. Figure 1b shows an order in the forest blueward of the quasar's  $\text{Ly}\alpha$  emission, where the accuracy of the sky subtraction may be gauged from the precision with which the bases of the saturated lines approach zero.

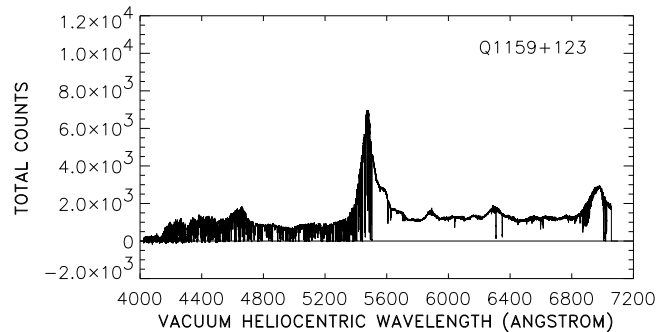


FIG. 3.—Complete spectrum of Q1159+123 formed by interpolating all the extracted orders to a uniform  $0.05 \text{ \AA}$  wavelength scale and then splicing adjacent orders. The principal feature is the quasar's  $\text{Ly}\alpha$  emission near  $5400 \text{ \AA}$ , and the spectrum extends just past C iv emission near  $7000 \text{ \AA}$ . There is a Lyman limit system near  $4150 \text{ \AA}$ . Most of the features longward of the  $\text{Ly}\alpha$  emission are C iv doublets, except for the atmospheric A band.

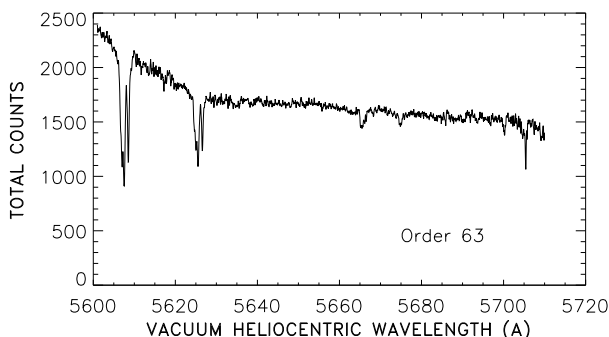


FIG. 2.—Final processed and extracted order in Q1159+123 for comparison with Fig. 1a. The total exposure of 8 hr is combined from a number of subexposures with spectra covering each order added in an S/N-optimized fashion.

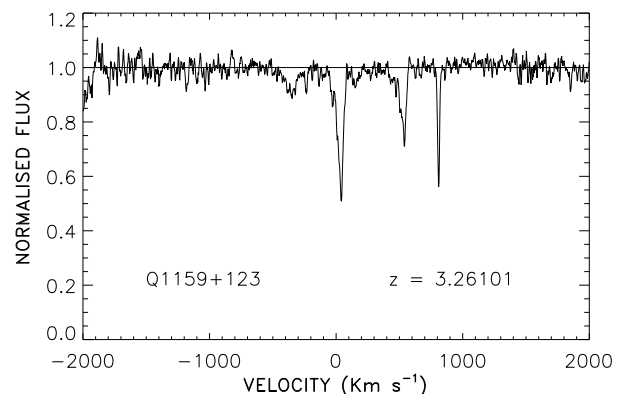


FIG. 4.—Typical continuum-fitted region of spectrum around the  $z = 3.26101$  C iv absorption-line complex in Q1159+123. The continuum was fitted to a  $\pm 2000 \text{ km s}^{-1}$  region around the C iv  $1548 \text{ \AA}$  line by iterating a second-order polynomial fit to a 10-point smoothed spectrum and rejecting significantly deviant regions.

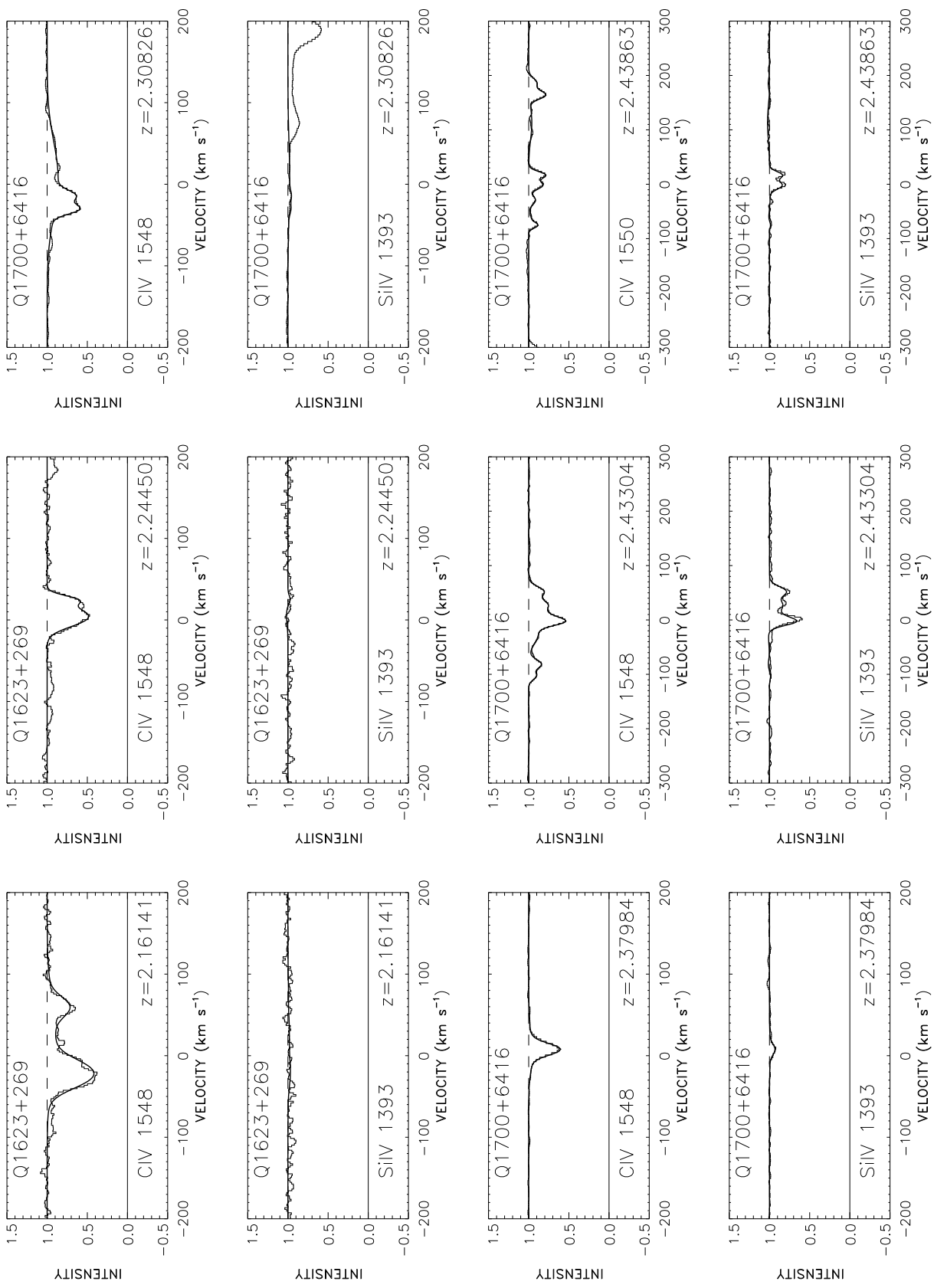


FIG. 5.—Voigt profile fits to the C IV and Si IV doublets in all cloud complexes in the sample with  $10^{13} \text{ cm}^{-2} < N(\text{C IV}) < 10^{14} \text{ cm}^{-2}$ . All doublets lie redward of the quasar's Ly $\alpha$  emission. Table 2 summarizes the redshifts, number of Voigt components, total C IV and Si IV column densities of each complex, and C II and Si II column densities.

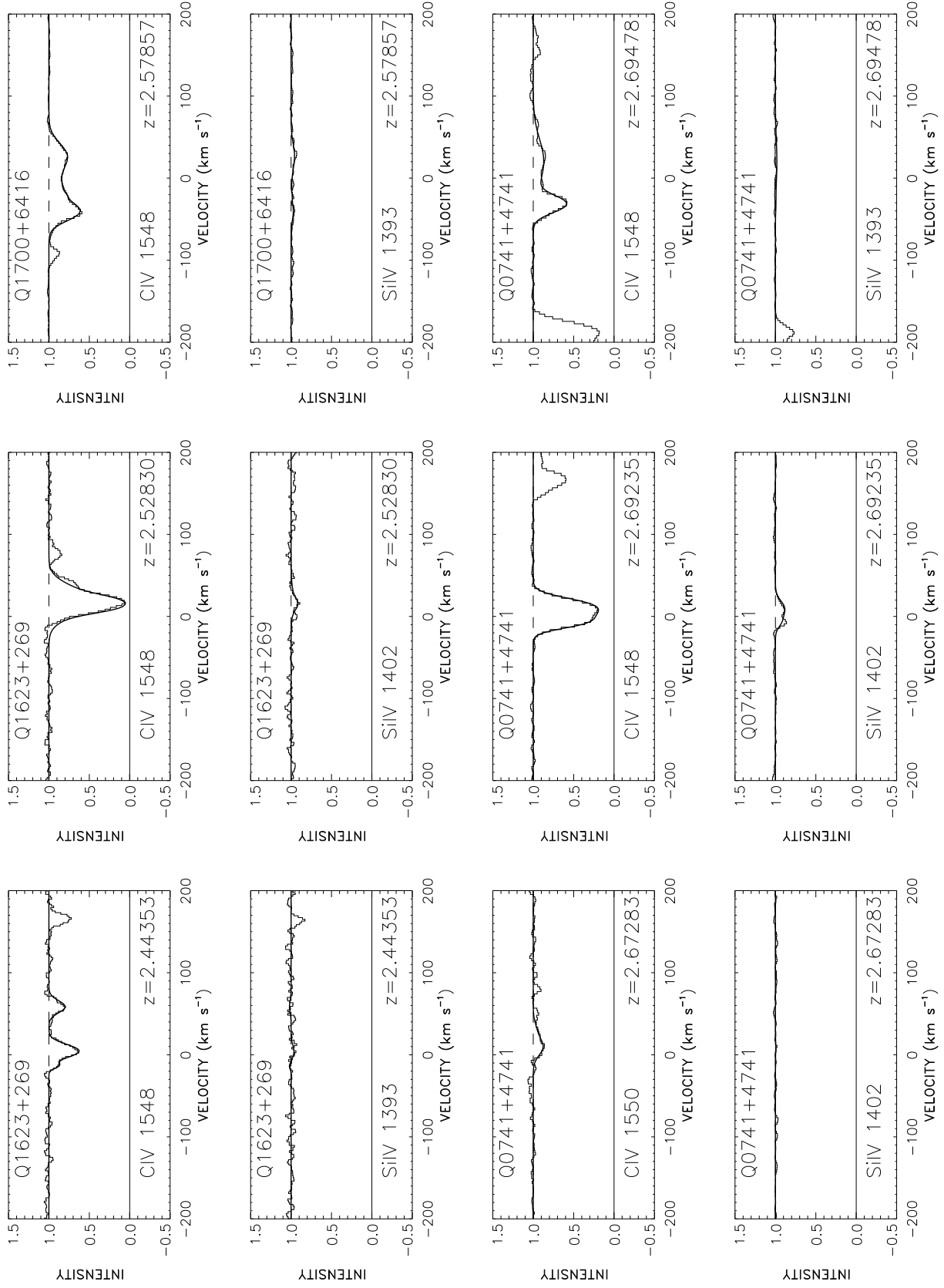


FIG. 5.—Continued

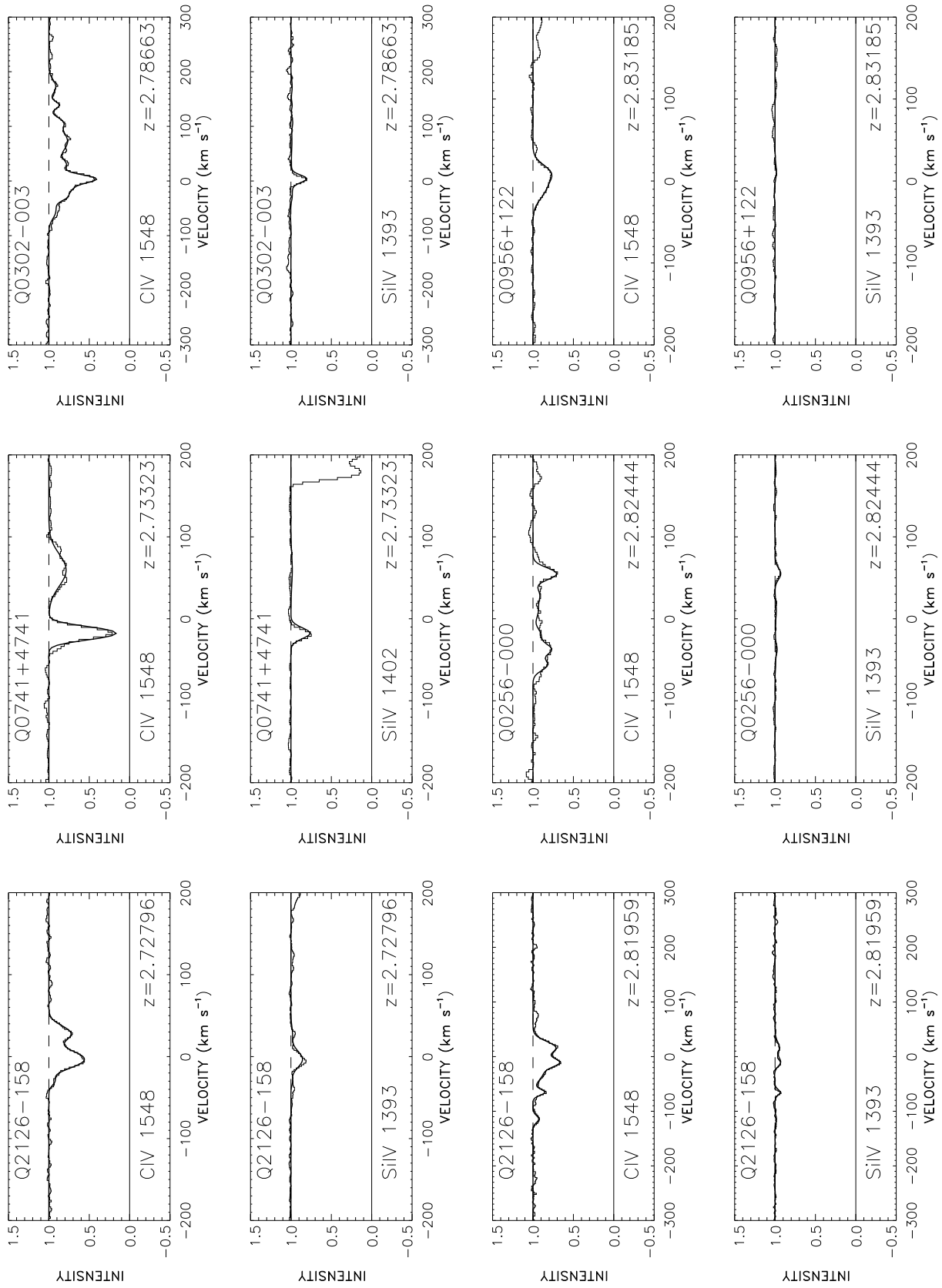


FIG. 5.—*Continued*

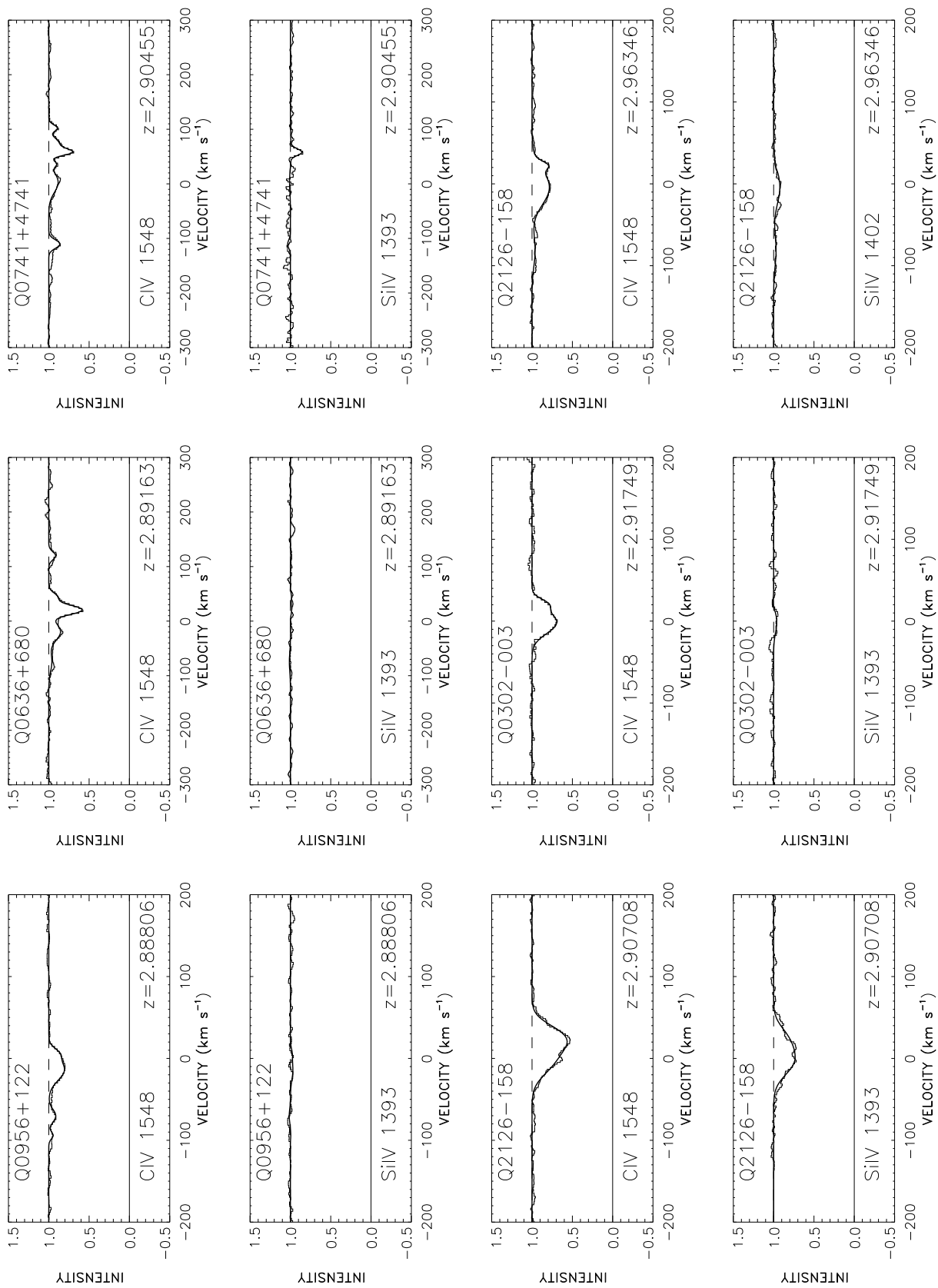


FIG. 5.—*Continued*

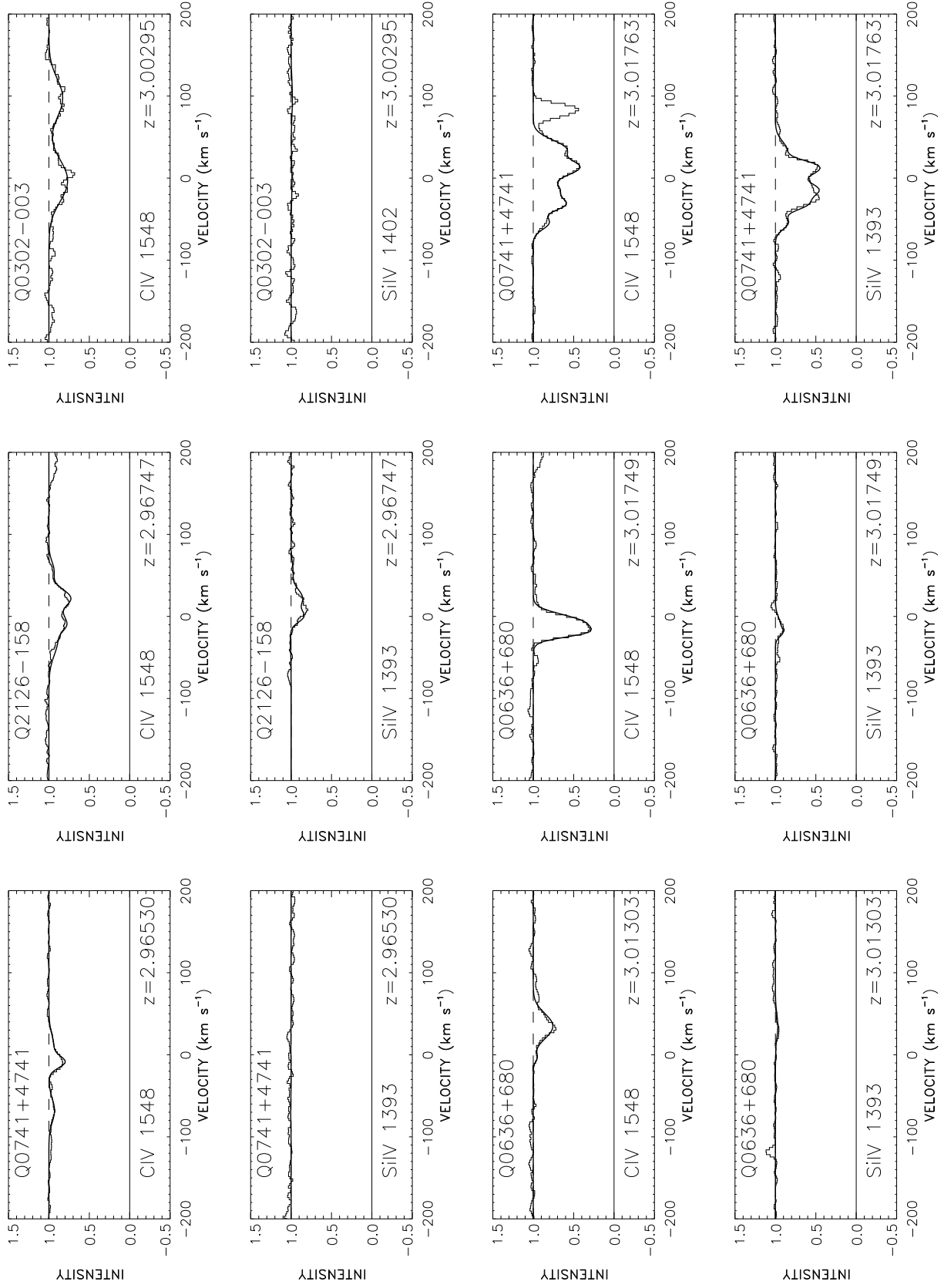


FIG. 5.—*Continued*



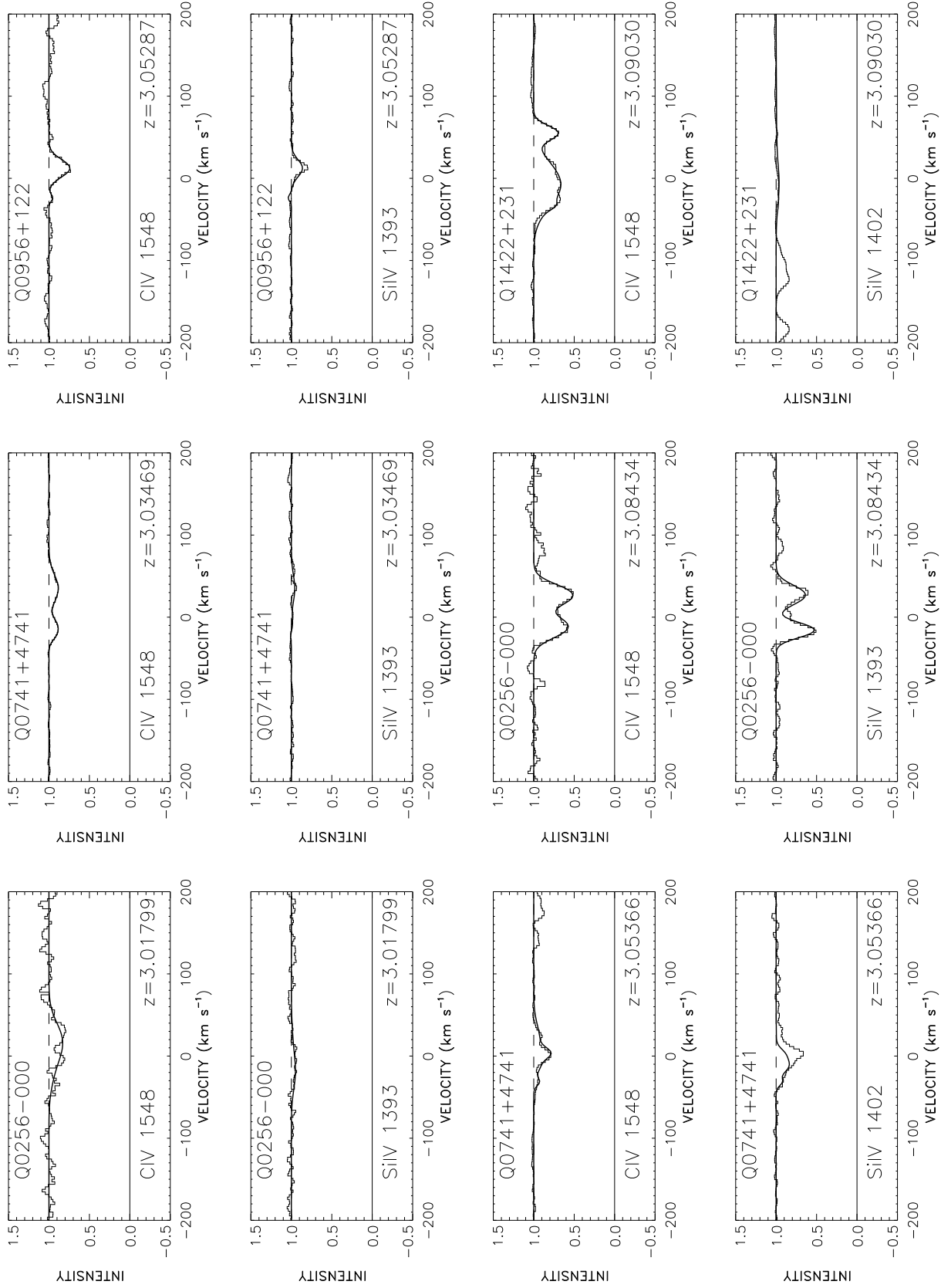


FIG. 5.—*Continued*

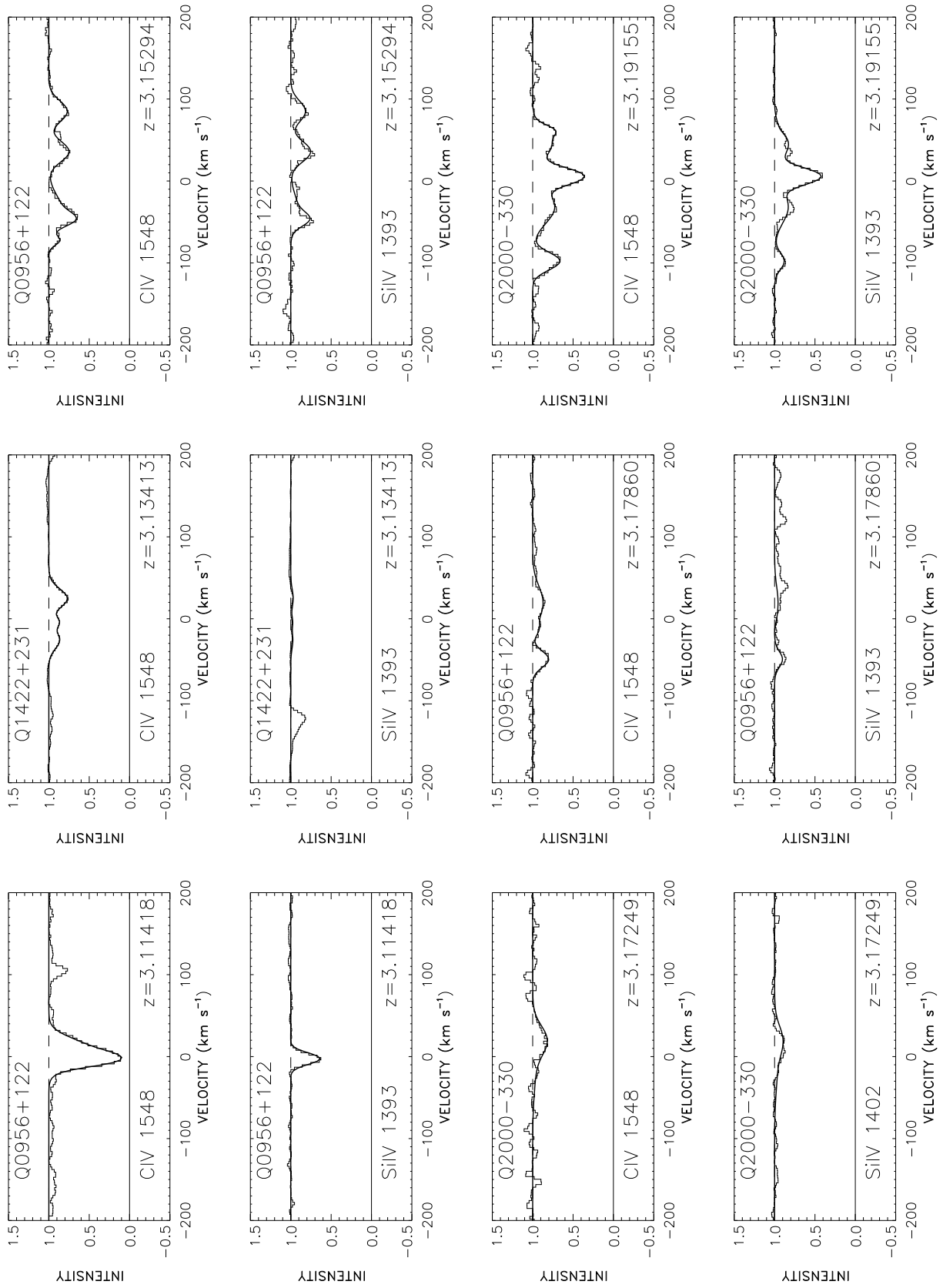


FIG. 5.—Continued

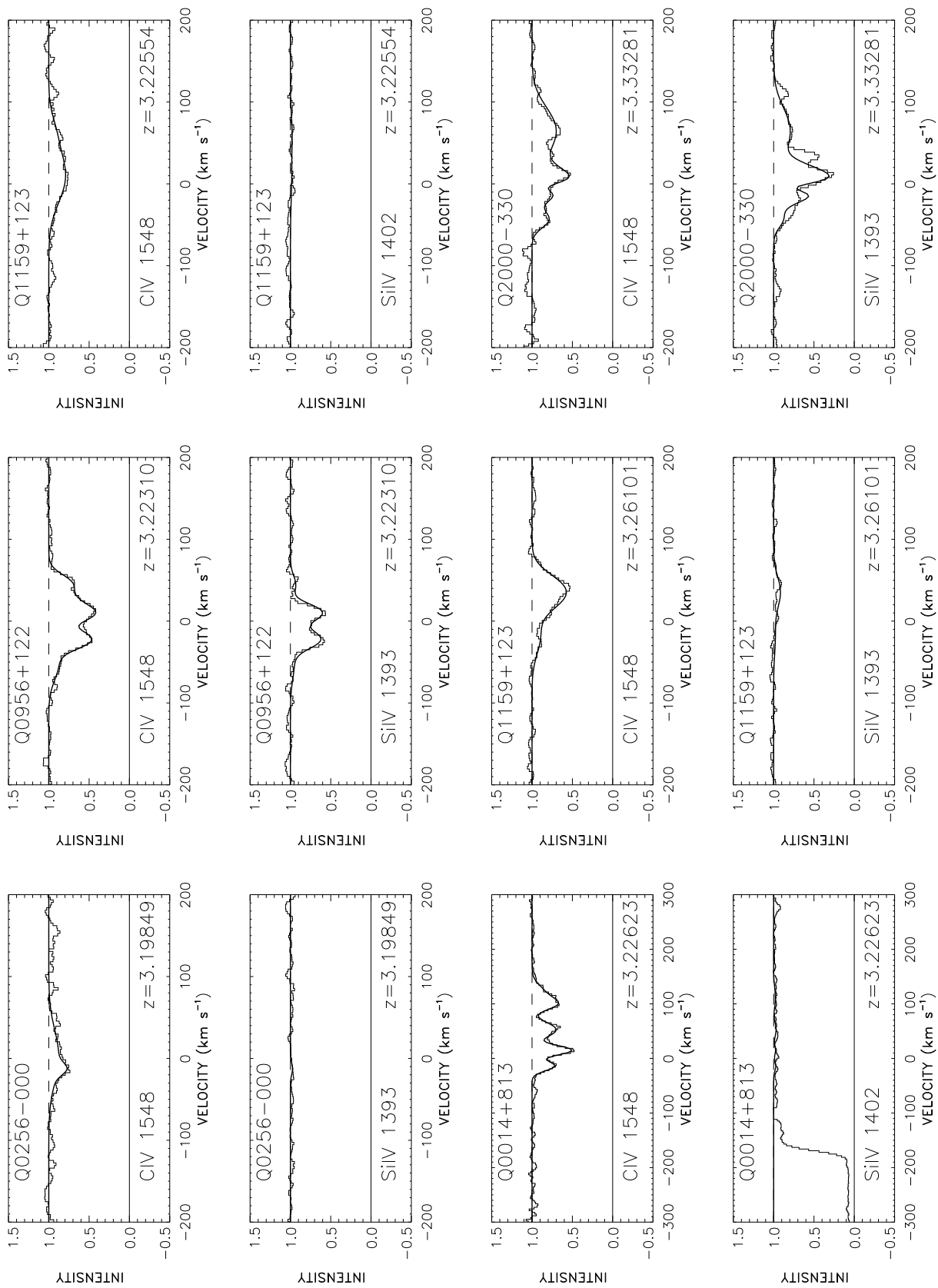


FIG. 5.—Continued

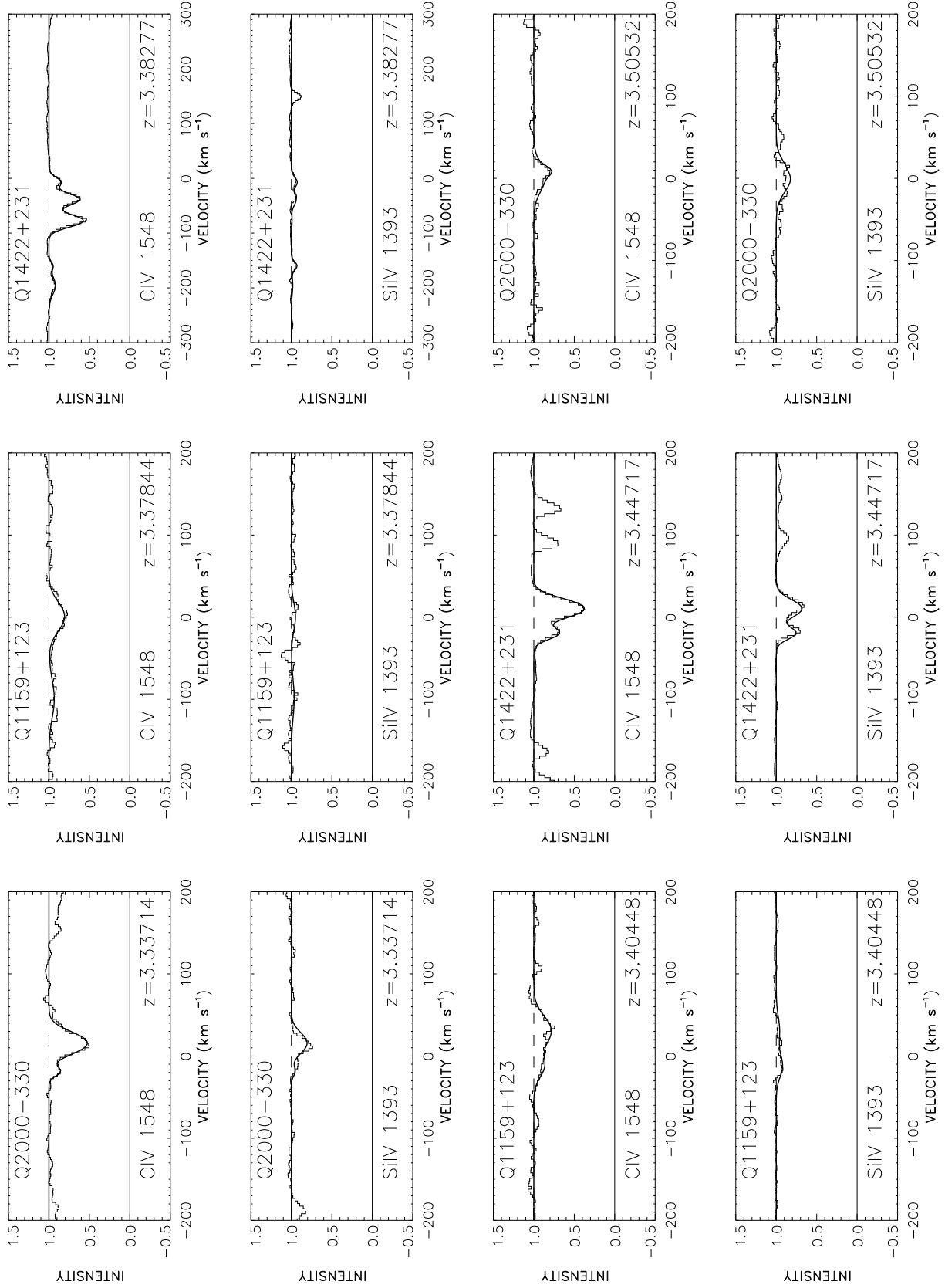


FIG. 5.—*Continued*

A final combined spectrum was made from all the observations taken at all echelle settings, with spectra covering each order added in an S/N-optimized fashion to form a combined spectrum of that order. The final 8 hr spectrum of order 63 in Q1159+123 is shown in Figure 2 for comparison with Figure 1a. An associated effective exposure time vector, normalized by the S/N, was also maintained at each point; this can be combined with the counts to determine the noise at each point in the spectrum. For some purposes it is useful to have a combined spectrum, and this was formed by interpolating all the orders to a uniform (0.05 Å) grid that provides Nyquist sampling throughout the wavelength range. A typical spectrum (of Q1159+123) is shown in Figure 3. This spectrum has a Lyman limit system just longward of 4150 Å and stretches through to C IV emission just below 7000 Å, near the atmospheric A band, which can be clearly seen in the spectrum. Most of the remaining features between Ly $\alpha$  and C IV emission are C IV absorption-line doublets.

For most purposes normalized (continuum-fitted) spectra from each order were used. The continuum fitting is made on a  $\pm 2000$  km s $^{-1}$  region of interest by iterating a second-order polynomial fit to a 10-point smoothed spectrum and rejecting significantly deviant regions ( $|\Delta \text{spectrum}/\text{fit}| > 0.025$ ). The fit to the region around a C IV complex at  $z = 3.26101$  in Q1159+123 is shown in Figure 4. Multiple Voigt profiles were then fitted to the absorption-line profiles using the IDL version of Bevington's CURVEFIT algorithm.

### 3. LINE RATIO EVOLUTION WITH REDSHIFT

#### 3.1. Introduction

Each quasar spectrum was first searched for all complexes of C IV doublets redward of the Ly $\alpha$  forest and outside of the quasar's proximity zone, defined to stretch to  $-4000$  km s $^{-1}$  blueward of the quasar's redshift. The sample was then restricted to those cases for which Si IV also lies redward of the quasar's Ly $\alpha$  emission. The redshift range used for each quasar is summarized in Table 1. Voigt pro-

files were next fitted to each such complex. The choice of the number of Voigt components is somewhat arbitrary because of the problems of blending, but the complexes are quite weak in general and, in the absence of saturation, the integrated column densities of complexes should be well determined. In the same way, integrated column densities or upper limits for Si IV, C II, and Si II were determined for lines lying longward of the forest. The usable redshift range for C II is also shown in Table 1. The profile fits to the C IV and Si IV doublets in all the cloud complexes with  $10^{13}$  cm $^{-2} < N(\text{C IV}) < 10^{14}$  cm $^{-2}$  are shown in Figure 5. The redshifts, number of Voigt components (a minimum of two were used), C IV column density, Si IV column density, and C II and Si II column densities (where these lines are redward of the forest) are summarized for all complexes with  $N(\text{C IV}) > 5 \times 10^{12}$  cm $^{-2}$  in Table 2.

#### 3.2. Evolution of Total Column Density Ratios

Figure 6 shows the evolution of the integrated value of Si IV/C IV in the 76 complexes with  $5 \times 10^{12}$  cm $^{-2} \leq N(\text{C IV}) \leq 10^{14}$  cm $^{-2}$ , as well as in the higher redshift systems satisfying this condition in the observations of Q0000–263 in Savaglio et al. (1997). As SC and Savaglio et al. (1997) previously noted, Si IV/C IV increases considerably between  $z = 2$  and  $z = 4$ , with a strong suggestion of a break in the distribution of values around  $z = 3$ . In contrast, the C II/C IV ratio displayed in Figure 7 does not exhibit this behavior: in most of the complexes in which C II/C IV can be measured, it is weak (C II/C IV  $< 0.1$ ) or undetected, regardless of redshift. Median values of Si IV/C IV are shown as a function of redshift in Figure 8. The median ratio is  $0.039^{+0.009}_{-0.006}$  for all the systems below  $z = 3$ , but  $0.13 \pm 0.04$  above  $z = 3$ , where the errors are  $1 \sigma$  computed using the median sign method. A key diagnostic in interpreting the data is whether the evolution is in the form of a step function or is a smoother change with redshift. A discontinuous change might arise from the effects of a change in the metagalactic ionizing spectrum at the He $^+$  ionization edge, whereas a smoother evolution might follow

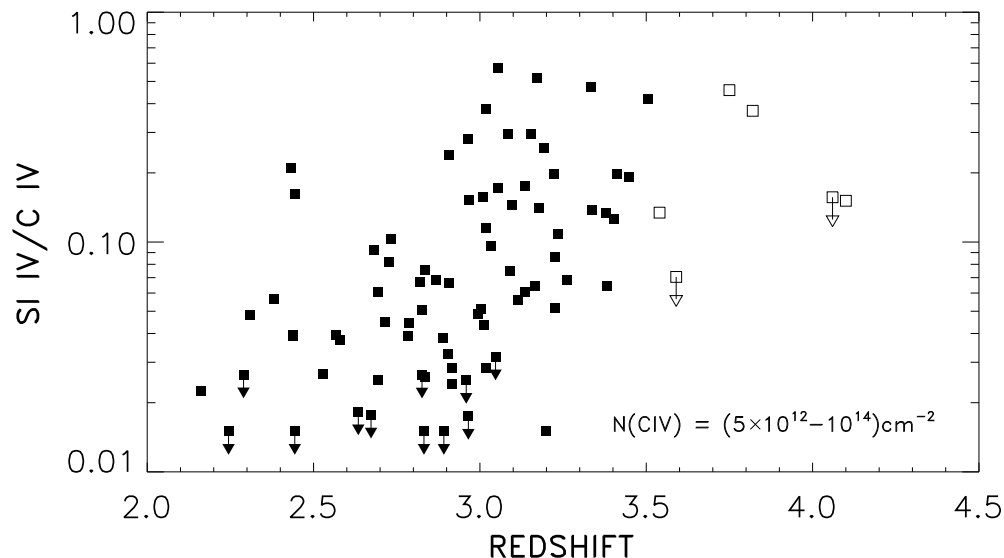


FIG. 6.—Ratio of total Si IV column density to total C IV column density as a function of redshift for the 76 complexes with  $5 \times 10^{12}$  cm $^{-2} \leq N(\text{C IV}) \leq 10^{14}$  cm $^{-2}$  (filled squares). Open squares denote values from Savaglio et al.'s (1997) observations of Q0000–263. Downward-pointing triangles show systems in which Si IV is not detected and where the points are positioned at the  $1 \sigma$  upper limit.

TABLE 2  
C IV, Si IV, C II, AND Si II COLUMN DENSITIES

<i>z</i>	Quasar	Number of Components	<i>N</i> (C iv) (cm <sup>-2</sup> )	<i>N</i> (Si iv) (cm <sup>-2</sup> )	<i>N</i> (C ii) (cm <sup>-2</sup> )	<i>N</i> (Si ii) (cm <sup>-2</sup> )
2.16141.....	1623+269	3	6.1 × 10 <sup>13</sup>	1.4 × 10 <sup>12</sup>	...	-1.9 × 10 <sup>11</sup>
2.24450.....	1623+269	2	3.1 × 10 <sup>13</sup>	-3.2 × 10 <sup>10</sup>	...	-2.4 × 10 <sup>11</sup>
2.28952.....	1700+6416	2	6.8 × 10 <sup>12</sup>	6.2 × 10 <sup>10</sup>	...	-2.6 × 10 <sup>11</sup>
2.30826.....	1700+6416	3	3.4 × 10 <sup>13</sup>	1.7 × 10 <sup>12</sup>	...	-9.5 × 10 <sup>11</sup>
2.31536.....	1700+6416	13	1.9 × 10 <sup>15</sup>	6.1 × 10 <sup>13</sup>	...	9.5 × 10 <sup>12</sup>
2.37984.....	1700+6416	2	1.3 × 10 <sup>13</sup>	7.3 × 10 <sup>11</sup>	...	4.6 × 10 <sup>11</sup>
2.40085.....	1623+269	5	1.2 × 10 <sup>14</sup>	-1.8 × 10 <sup>11</sup>	9.7 × 10 <sup>10</sup>	4.5 × 10 <sup>11</sup>
2.43304.....	1700+6416	7	4.3 × 10 <sup>13</sup>	9.0 × 10 <sup>12</sup>	...	-1.2 × 10 <sup>11</sup>
2.43814.....	2347-4342	2	7.5 × 10 <sup>12</sup>	3.0 × 10 <sup>11</sup>	...	-3.4 × 10 <sup>10</sup>
2.43863.....	1700+6416	8	5.2 × 10 <sup>13</sup>	2.0 × 10 <sup>12</sup>	2.6 × 10 <sup>11</sup>	-1.3 × 10 <sup>12</sup>
2.44353.....	1623+269	3	1.7 × 10 <sup>13</sup>	6.8 × 10 <sup>10</sup>	-3.1 × 10 <sup>12</sup>	-1.2 × 10 <sup>12</sup>
2.44534.....	1623+269	2	6.3 × 10 <sup>12</sup>	1.0 × 10 <sup>12</sup>	2.7 × 10 <sup>12</sup>	1.4 × 10 <sup>10</sup>
2.56817.....	1700+6416	2	6.6 × 10 <sup>12</sup>	2.6 × 10 <sup>11</sup>	-5.5 × 10 <sup>10</sup>	2.0 × 10 <sup>10</sup>
2.57857.....	1700+6416	4	3.6 × 10 <sup>13</sup>	1.3 × 10 <sup>12</sup>	1.9 × 10 <sup>12</sup>	-3.6 × 10 <sup>11</sup>
2.63449.....	2347-4342	2	9.9 × 10 <sup>12</sup>	1.8 × 10 <sup>10</sup>	9.9 × 10 <sup>12</sup>	-3.0 × 10 <sup>11</sup>
2.67283.....	0741+4741	2	1.0 × 10 <sup>13</sup>	8.7 × 10 <sup>10</sup>	...	1.3 × 10 <sup>11</sup>
2.68228.....	0636+680	2	8.4 × 10 <sup>12</sup>	7.8 × 10 <sup>11</sup>	...	1.0 × 10 <sup>12</sup>
2.69235.....	0741+4741	2	6.5 × 10 <sup>13</sup>	4.0 × 10 <sup>12</sup>	...	-2.7 × 10 <sup>11</sup>
2.69478.....	0741+4741	2	2.7 × 10 <sup>13</sup>	6.8 × 10 <sup>11</sup>	...	-5.5 × 10 <sup>11</sup>
2.71446.....	0741+4741	2	6.3 × 10 <sup>12</sup>	2.8 × 10 <sup>11</sup>	...	1.9 × 10 <sup>11</sup>
2.72796.....	2126-158	3	2.8 × 10 <sup>13</sup>	2.3 × 10 <sup>12</sup>	...	-6.1 × 10 <sup>11</sup>
2.73323.....	0741+4741	2	5.1 × 10 <sup>13</sup>	5.3 × 10 <sup>12</sup>	...	-1.1 × 10 <sup>12</sup>
2.73564.....	2347-4342	5	1.1 × 10 <sup>14</sup>	1.9 × 10 <sup>13</sup>	6.8 × 10 <sup>12</sup>	4.8 × 10 <sup>10</sup>
2.76916.....	2126-158	12	4.6 × 10 <sup>14</sup>	6.4 × 10 <sup>13</sup>	...	6.5 × 10 <sup>14</sup>
2.78488.....	0741+4741	2	1.0 × 10 <sup>13</sup>	3.9 × 10 <sup>11</sup>	...	-1.6 × 10 <sup>11</sup>
2.78663.....	0302-003	9	7.1 × 10 <sup>13</sup>	3.1 × 10 <sup>12</sup>	...	4.9 × 10 <sup>11</sup>
2.81959.....	2126-158	5	3.0 × 10 <sup>13</sup>	2.0 × 10 <sup>12</sup>	...	1.7 × 10 <sup>11</sup>
2.82444.....	0256-000	6	2.3 × 10 <sup>13</sup>	1.2 × 10 <sup>12</sup>	...	-7.1 × 10 <sup>11</sup>
2.82593.....	0302-003	2	6.8 × 10 <sup>12</sup>	-2.4 × 10 <sup>11</sup>	...	2.1 × 10 <sup>11</sup>
2.83185.....	0956+122	2	1.3 × 10 <sup>13</sup>	8.3 × 10 <sup>10</sup>	...	-6.9 × 10 <sup>11</sup>
2.83433.....	0956+122	2	8.9 × 10 <sup>12</sup>	2.3 × 10 <sup>11</sup>	...	-2.1 × 10 <sup>11</sup>
2.83599.....	0256-000	2	5.6 × 10 <sup>12</sup>	4.2 × 10 <sup>11</sup>	...	8.0 × 10 <sup>11</sup>
2.86883.....	0636+680	2	7.3 × 10 <sup>12</sup>	5.0 × 10 <sup>11</sup>	-3.9 × 10 <sup>11</sup>	4.7 × 10 <sup>11</sup>
2.88806.....	0956+122	4	1.3 × 10 <sup>13</sup>	5.1 × 10 <sup>11</sup>	...	1.1 × 10 <sup>12</sup>
2.89163.....	0636+680	5	2.8 × 10 <sup>13</sup>	5.6 × 10 <sup>10</sup>	4.5 × 10 <sup>9</sup>	-6.6 × 10 <sup>11</sup>
2.90374.....	0636+680	9	3.0 × 10 <sup>14</sup>	1.4 × 10 <sup>14</sup>	4.3 × 10 <sup>14</sup>	5.5 × 10 <sup>13</sup>
2.90455.....	0741+4741	6	2.4 × 10 <sup>13</sup>	7.8 × 10 <sup>11</sup>	2.2 × 10 <sup>12</sup>	-1.4 × 10 <sup>12</sup>
2.90708.....	2126-158	2	3.6 × 10 <sup>13</sup>	8.7 × 10 <sup>12</sup>	5.5 × 10 <sup>12</sup>	-3.1 × 10 <sup>11</sup>
2.90823.....	0014+813	2	6.8 × 10 <sup>12</sup>	4.5 × 10 <sup>11</sup>	...	6.5 × 10 <sup>11</sup>
2.91490.....	0956+122	2	8.7 × 10 <sup>12</sup>	2.1 × 10 <sup>11</sup>	...	-3.4 × 10 <sup>8</sup>
2.91749.....	0302-003	2	1.8 × 10 <sup>13</sup>	5.0 × 10 <sup>11</sup>	1.3 × 10 <sup>12</sup>	4.0 × 10 <sup>11</sup>
2.95882.....	0302-003	2	7.2 × 10 <sup>12</sup>	1.1 × 10 <sup>11</sup>	-1.1 × 10 <sup>12</sup>	-3.5 × 10 <sup>11</sup>
2.96346.....	2126-158	3	2.0 × 10 <sup>13</sup>	5.5 × 10 <sup>12</sup>	1.6 × 10 <sup>11</sup>	9.8 × 10 <sup>11</sup>
2.96530.....	0741+4741	3	1.0 × 10 <sup>13</sup>	-1.3 × 10 <sup>11</sup>	2.6 × 10 <sup>11</sup>	6.7 × 10 <sup>11</sup>
2.96747.....	2126-158	5	2.5 × 10 <sup>13</sup>	3.8 × 10 <sup>12</sup>	9.1 × 10 <sup>12</sup>	7.0 × 10 <sup>11</sup>
2.99540.....	0302-003	2	6.6 × 10 <sup>12</sup>	3.2 × 10 <sup>11</sup>	-1.9 × 10 <sup>12</sup>	-2.4 × 10 <sup>11</sup>
3.00295.....	0302-003	2	3.3 × 10 <sup>13</sup>	1.7 × 10 <sup>12</sup>	7.4 × 10 <sup>11</sup>	1.2 × 10 <sup>12</sup>
3.01043.....	0956+122	2	9.7 × 10 <sup>12</sup>	1.5 × 10 <sup>12</sup>	3.8 × 10 <sup>12</sup>	-1.0 × 10 <sup>12</sup>
3.01303.....	0636+680	2	1.3 × 10 <sup>13</sup>	5.8 × 10 <sup>11</sup>	-1.4 × 10 <sup>12</sup>	-7.8 × 10 <sup>11</sup>
3.01749.....	0636+680	2	4.1 × 10 <sup>13</sup>	1.2 × 10 <sup>12</sup>	7.0 × 10 <sup>11</sup>	-4.1 × 10 <sup>9</sup>
3.01763.....	0741+4741	6	6.6 × 10 <sup>13</sup>	2.5 × 10 <sup>13</sup>	1.1 × 10 <sup>15</sup>	1.5 × 10 <sup>14</sup>
3.01799.....	0256-000	2	1.5 × 10 <sup>13</sup>	1.7 × 10 <sup>12</sup>	4.3 × 10 <sup>10</sup>	-1.2 × 10 <sup>12</sup>
3.03469.....	0741+4741	3	1.0 × 10 <sup>13</sup>	9.7 × 10 <sup>11</sup>	5.9 × 10 <sup>10</sup>	-2.3 × 10 <sup>11</sup>
3.04705.....	0302-003	2	5.7 × 10 <sup>12</sup>	-8.7 × 10 <sup>10</sup>	3.2 × 10 <sup>11</sup>	-5.7 × 10 <sup>10</sup>
3.05287.....	0956+122	2	1.0 × 10 <sup>13</sup>	1.8 × 10 <sup>12</sup>	-3.3 × 10 <sup>11</sup>	6.1 × 10 <sup>10</sup>
3.05366.....	0741+4741	4	1.1 × 10 <sup>13</sup>	6.3 × 10 <sup>12</sup>	-1.7 × 10 <sup>12</sup>	1.7 × 10 <sup>11</sup>
3.08434.....	0256-000	2	4.5 × 10 <sup>13</sup>	1.3 × 10 <sup>13</sup>	6.6 × 10 <sup>12</sup>	1.7 × 10 <sup>11</sup>
3.09030.....	1422+231	4	4.2 × 10 <sup>13</sup>	3.1 × 10 <sup>12</sup>	...	-1.3 × 10 <sup>11</sup>
3.09691.....	0956+122	2	7.1 × 10 <sup>12</sup>	1.0 × 10 <sup>12</sup>	1.5 × 10 <sup>12</sup>	8.6 × 10 <sup>11</sup>
3.11418.....	0956+122	2	6.9 × 10 <sup>13</sup>	3.9 × 10 <sup>12</sup>	1.2 × 10 <sup>12</sup>	-5.2 × 10 <sup>11</sup>
3.13413.....	1422+231	3	1.6 × 10 <sup>13</sup>	9.7 × 10 <sup>11</sup>	...	-3.3 × 10 <sup>10</sup>
3.13702.....	1422+231	2	6.2 × 10 <sup>12</sup>	1.1 × 10 <sup>12</sup>	...	5.3 × 10 <sup>11</sup>
3.15294.....	0956+122	5	3.9 × 10 <sup>13</sup>	1.2 × 10 <sup>13</sup>	4.2 × 10 <sup>12</sup>	3.3 × 10 <sup>11</sup>
3.16701.....	1159+123	2	8.6 × 10 <sup>12</sup>	5.5 × 10 <sup>11</sup>	-3.6 × 10 <sup>11</sup>	1.5 × 10 <sup>11</sup>
3.17249.....	2000-330	2	1.3 × 10 <sup>13</sup>	6.7 × 10 <sup>12</sup>	...	2.1 × 10 <sup>12</sup>
3.17860.....	0956+122	3	1.6 × 10 <sup>13</sup>	2.3 × 10 <sup>12</sup>	8.8 × 10 <sup>11</sup>	-3.0 × 10 <sup>11</sup>
3.19155.....	2000-330	5	7.6 × 10 <sup>13</sup>	1.9 × 10 <sup>13</sup>	...	6.2 × 10 <sup>13</sup>
3.19849.....	0256-000	2	1.6 × 10 <sup>13</sup>	2.4 × 10 <sup>11</sup>	6.3 × 10 <sup>11</sup>	2.6 × 10 <sup>11</sup>
3.22310.....	0956+122	5	7.5 × 10 <sup>13</sup>	1.5 × 10 <sup>13</sup>	2.0 × 10 <sup>12</sup>	1.9 × 10 <sup>11</sup>
3.22554.....	1159+123	2	2.6 × 10 <sup>13</sup>	2.2 × 10 <sup>12</sup>	-1.3 × 10 <sup>12</sup>	-2.7 × 10 <sup>11</sup>
3.22623.....	0014+813	5	5.8 × 10 <sup>13</sup>	3.0 × 10 <sup>12</sup>	-1.6 × 10 <sup>12</sup>	-1.3 × 10 <sup>12</sup>
3.23339.....	0014+813	2	9.6 × 10 <sup>12</sup>	1.0 × 10 <sup>12</sup>	2.0 × 10 <sup>11</sup>	7.0 × 10 <sup>10</sup>
3.26101.....	1159+123	2	3.8 × 10 <sup>13</sup>	2.6 × 10 <sup>12</sup>	-4.0 × 10 <sup>11</sup>	7.6 × 10 <sup>11</sup>
3.33281.....	2000-330	4	6.2 × 10 <sup>13</sup>	2.9 × 10 <sup>13</sup>	...	3.8 × 10 <sup>12</sup>
3.33714.....	2000-330	2	2.7 × 10 <sup>13</sup>	3.7 × 10 <sup>12</sup>	...	8.2 × 10 <sup>11</sup>
3.37844.....	1159+123	2	1.6 × 10 <sup>13</sup>	2.2 × 10 <sup>12</sup>	1.3 × 10 <sup>11</sup>	-5.2 × 10 <sup>9</sup>
3.38277.....	1422+231	5	4.4 × 10 <sup>13</sup>	2.8 × 10 <sup>12</sup>	2.1 × 10 <sup>12</sup>	3.7 × 10 <sup>11</sup>
3.40448.....	1159+123	2	1.9 × 10 <sup>13</sup>	2.3 × 10 <sup>12</sup>	-6.8 × 10 <sup>11</sup>	3.5 × 10 <sup>11</sup>
3.41121.....	1422+231	2	8.7 × 10 <sup>12</sup>	1.7 × 10 <sup>12</sup>	4.7 × 10 <sup>10</sup>	7.9 × 10 <sup>10</sup>
3.44717.....	1422+231	2	4.0 × 10 <sup>13</sup>	7.6 × 10 <sup>12</sup>	-4.0 × 10 <sup>10</sup>	3.9 × 10 <sup>10</sup>
3.50532.....	2000-330	2	9.7 × 10 <sup>12</sup>	4.1 × 10 <sup>12</sup>	2.6 × 10 <sup>12</sup>	2.3 × 10 <sup>10</sup>
3.53863.....	1422+231	11	1.8 × 10 <sup>14</sup>	3.8 × 10 <sup>13</sup>	4.4 × 10 <sup>13</sup>	2.4 × 10 <sup>12</sup>
3.54937.....	2000-330	11	2.3 × 10 <sup>14</sup>	6.3 × 10 <sup>13</sup>	1.7 × 10 <sup>14</sup>	9.4 × 10 <sup>12</sup>

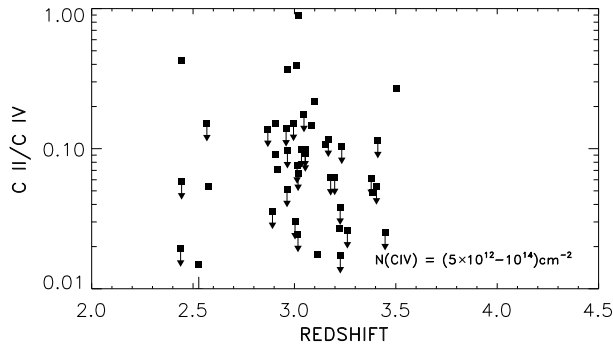


FIG. 7.—Ratio of total C II column density to total C IV column density as a function of redshift for the complexes of Fig. 6 in which the C II system lies longer in wavelength than the forest. Downward-pointing triangles show systems in which C II is not detected and where the points are positioned at the  $1\sigma$  upper limit.

from the more general evolution of the external ionizing field and the range of internal densities and internal ionization in the complexes. The data of Figures 6 and 8 are strongly suggestive of an abrupt transition between  $z = 2.9$  and  $z = 3$ . This redshift is slightly higher than, but comparable to, the redshift ( $z = 2.8$ – $2.9$ ) below which He II would be inferred to be predominantly ionized to He III from the direct observations of the He II Ly $\alpha$  forest (Reimers et al. 1997).

To quantify this, distribution functions of Si IV/C IV have been formed for complexes with  $z = 2.75$ – $2.95$ , just below the suspected break, and for  $z = 3.0$ – $3.2$ , just above it. The histograms representing Si IV/C IV values for the 16 systems in the low-redshift interval and the 22 systems in the high-redshift interval are shown in Figure 9. The median value of  $0.038^{+0.029}_{-0.010}$  at  $2.75 < z < 2.95$  is consistent with that of all the  $z < 3$  systems, whereas the  $3.0 < z < 3.2$  median value of  $0.14^{+0.04}_{-0.075}$  is consistent with that of all the  $z > 3$  systems. Moreover, a rank sum test shows that the  $z = 2.75$ – $2.95$  data are consistent with being drawn from the same distribution as the  $z < 2.75$  systems, and the  $z = 3.0$ – $3.2$  data with being drawn from the same distribution as the  $z > 3.2$  systems. However, the rank sum test shows that the  $z = 3.0$ – $3.2$  data have a probability of only  $2.2 \times 10^{-4}$  of being drawn from the same distribution as the  $z = 2.75$ – $2.95$  data, and that at the 98% confidence level the data require a jump of at least a multiplicative factor of 1.8 from

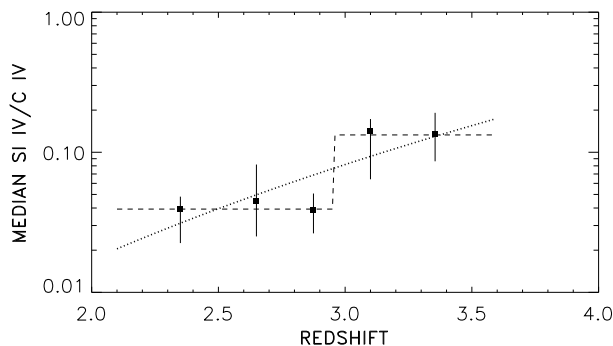


FIG. 8.—Median values of Si IV/C IV as a function of redshift for the sample of Fig. 6. Errors are  $\pm 1\sigma$  computed using the median sign method. The median value of Si IV/C IV is  $0.039^{+0.009}_{-0.006}$  for  $z < 3$  and  $0.13 \pm 0.04$  for  $z > 3$ . The dashed line is a step function fit to the data, with a jump of a factor of 3.4 at  $z = 2.95$ . The dotted line has the form  $(1+z)^{5.4}$ . It does not predict a sufficient jump between  $z = 2.85$  and  $z = 3.1$  to reconcile the low- and high-redshift distributions (Fig. 9).

the lower to the higher redshift interval. The data are therefore consistent with invariant distributions at high and low redshift together with an abrupt jump between  $z = 2.9$  and  $z = 3$ . The corresponding step function, with Si IV/C IV changing by a factor of 3.4 at  $z = 2.95$ , is shown as the dashed line in Figure 8.

Assuming instead that the evolution of the median ionization ratio is a smooth power law in  $1+z$  requires an evolution of the form  $(1+z)^{5.4}$ , which is shown as the dotted line in Figure 8. This however predicts a jump of only 1.57 between  $z = 2.85$  and  $z = 3.1$  which, as already noted, is not large enough to reconcile the relative distribution functions of Figure 9. It would therefore seem that simple smooth power-law evolution is not consistent with the data.

### 3.3. Internal Structure

Variations of the ionization ratios in different regions within a complex can result from structure in the internal density of material in the complex or from the presence of internal ionization sources. It is therefore of considerable interest to examine the ionization ratios within the complexes to understand how these effects can contribute to the overall ionization balance and to determine whether or not this can change the conclusions of § 3.2.

The simplest approach to this is to break down the complexes into the components determined by Voigt profile fitting (Boksenberg 1998). Figure 10 shows the redshift evolution of the Si IV/C IV components broken down in this way. All components with  $N(\text{C IV}) > 5 \times 10^{12} \text{ cm}^{-2}$  have been included irrespective of the total column density of the complex, so that a small number of high-density complexes provide a large number of components, and these also include a number of Lyman limit systems in which radiative transfer effects are significant. However, even with these effects and with the increased confusion owing to the large spread in components, the change between high and low redshifts is clearly seen. Figure 11 shows histograms of the distributions above and below  $z = 3$ . If the components are considered to be statistically independent samples, then the

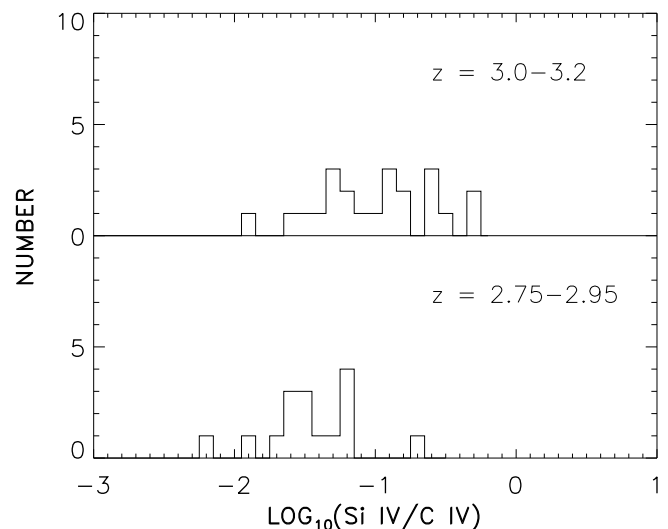


FIG. 9.—Histograms of the distributions of  $\log(\text{Si IV/C IV})$  for 22 systems with  $z = 3.0$ – $3.2$  (top) with a median of  $0.14^{+0.04}_{-0.075}$  and 16 systems with  $z = 2.75$ – $2.95$  (bottom) with a median of  $0.038^{+0.029}_{-0.010}$ . A multiplicative jump of at least a factor of 1.8 is required at the 98% confidence level to reconcile the low- and high-redshift distributions.

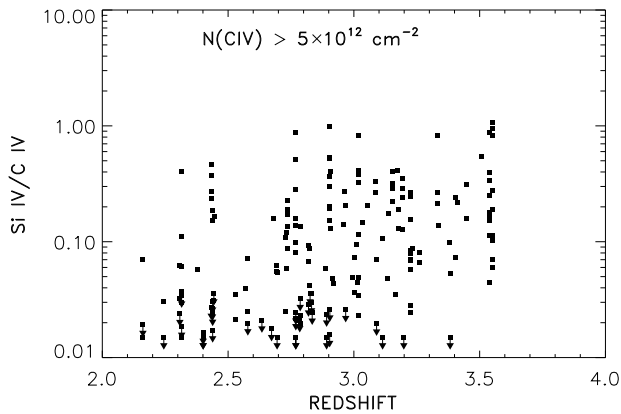


FIG. 10.—Si IV/C IV as a function of redshift for all Voigt profile components with  $N(\text{C IV}) > 5 \times 10^{12} \text{ cm}^{-2}$  in the sample irrespective of the total column density of the complex and including a number of Lyman limit systems.

median ratio is  $0.043^{+0.015}_{-0.008}$  below  $z = 3$  and  $0.15 \pm 0.04$  above  $z = 3$ . At the 98% confidence level, the minimum multiplicative increase to bring the distributions into consistency is 1.93.

However, the methodology of fitting Voigt profiles is a very unsatisfactory approach to this problem because of the considerable arbitrariness in the choice of components, which can have several unfortunate effects, including forcing other ions preferentially into or out of a particular component, blending components, and introducing nonindependent components. These problems can be avoided by using the more direct technique of computing the ratios of the optical depths of various ions throughout the complex. This procedure is illustrated in Figures 12 and 13. For each identified C IV complex, all data points lying above some limiting optical depth [here  $\tau(\text{C IV } \lambda 1550) > 0.05$ ] were identified, and optical depths in the corresponding regions of the other ions were then measured. Si IV and C IV optical depths for a complex at  $z = 3.33714$  in Q2000–330 are shown in Figure 12. The ratio  $(\tau\lambda f)$  relative to that of C IV then yields the ratio of  $N(\text{ion})/N(\text{C IV})$  throughout the velocity range of the complex, as is illustrated in Figure 13, where

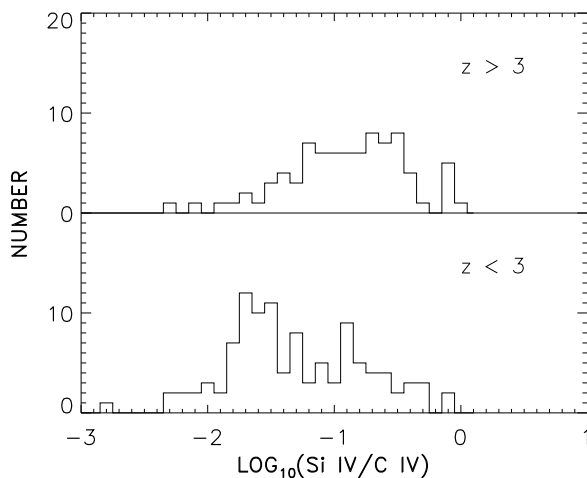


FIG. 11.—Histograms of the distributions of  $\log(\text{Si IV/C IV})$  for all Voigt profile components in the sample of Fig. 10 with  $z > 3$  (top) with a median of  $0.15 \pm 0.04$  and for  $z < 3$  (bottom) with a median of  $0.043^{+0.015}_{-0.008}$ . A multiplicative jump of a least a factor of 1.93 is required at the 98% confidence level to reconcile the low- and high-redshift distributions.

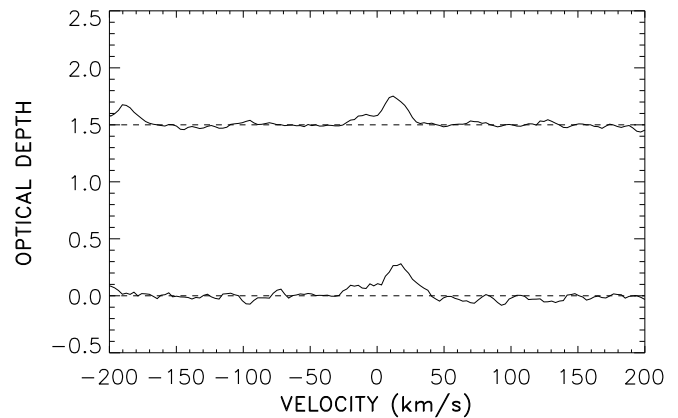


FIG. 12.—Sample optical depths of Si IV (top) and C IV (bottom) for the  $z = 3.33714$  complex in Q2000–330. The Si IV optical depth has been offset by 1.5.

it is compared with the average ion ratios in the complex (solid line). This procedure can be slightly in error if there is a substantial amount of thermal broadening but should be adequate for these heavier elements where the broadening is primarily kinematic. Si IV/C IV values determined in this way for all the complexes of Table 2 are shown in Figure 14, in which again a clear evolution of the distribution can be seen.

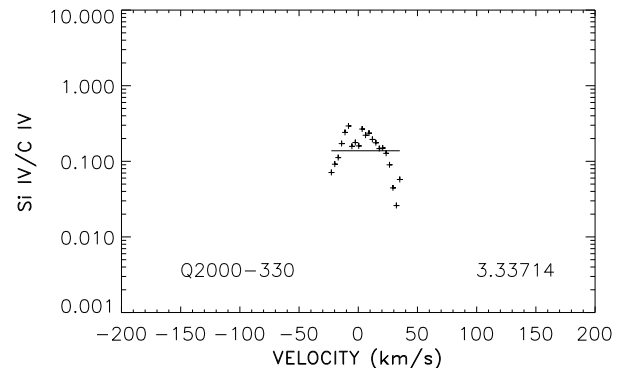


FIG. 13.—Si IV/C IV values across the  $z = 3.33714$  complex in Q2000–330, computed from the Si IV and C IV optical depths of Fig. 12 with  $\tau(\text{C IV}) > 0.05$ , as  $N(\text{ion}) = \tau\lambda f$ , where  $\lambda$  is the wavelength and  $f$  is the oscillator strength of the transition. The solid line is the average value of Si IV/C IV in the complex, computed from the total column densities of Si IV and C IV measured from Voigt profile fitting.

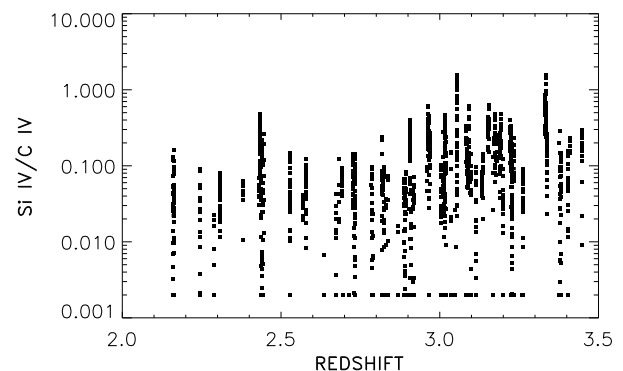


FIG. 14.—Si IV/C IV density ratios computed from optical depths as in Fig. 13 for all the absorption-line complexes of Table 2, as a function of the redshift of the complex.



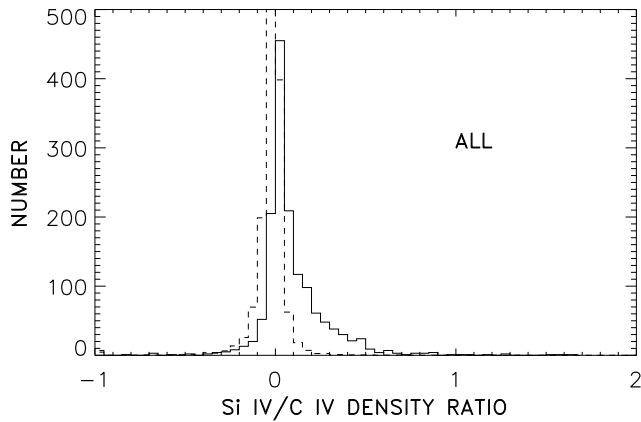


FIG. 15a

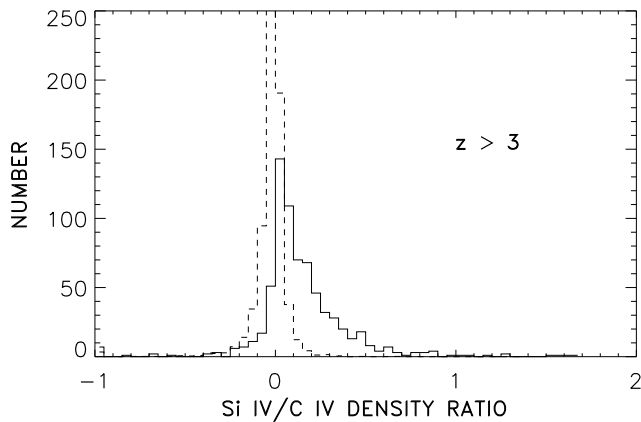


FIG. 15b

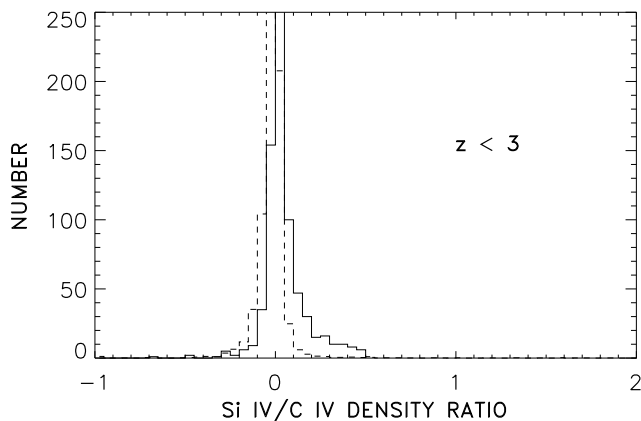


FIG. 15c

FIG. 15.—(a) Distribution of Si IV/C IV density ratios for all the data of Fig. 14 (solid line) compared with the average of random realizations (dashed line). (b) Same as (a), but for  $z > 3$ . (c) Same as (a), but for  $z < 3$ . Median and mean values and  $1\sigma$  errors are given in Tables 3 and 4, respectively.

In order to determine the noise levels associated with this procedure, a large number of blank-field realizations were constructed, in which the redshift was slightly displaced from the true value. This Monte Carlo technique is extremely powerful, providing an unbiased measure of the noise, including the systematic effects of continuum uncertainty, varying S/N among the quasars and within a single quasar spectrum, and contamination by unidentified absorption lines. Indeed, this last named property allows a

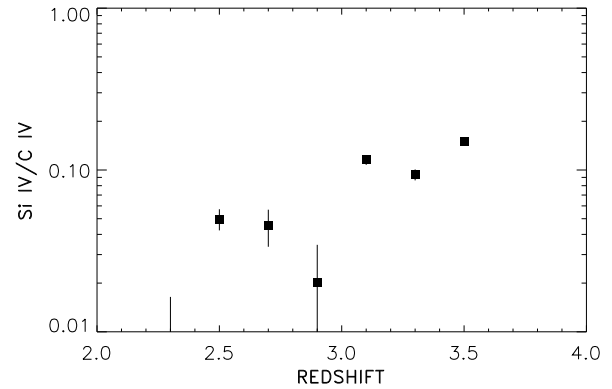


FIG. 16.—Median Si IV/C IV as a function of redshift for the data of Fig. 14 with  $\pm 1\sigma$  errors. The median is  $0.035 \pm 0.005$  for  $z < 3$  and  $0.10 \pm 0.01$  for  $z > 3$ .

robust measure (§ 4) of the average column densities of ions lying in the Ly $\alpha$  forest.

In Figure 15, the measured distribution (solid line) of Si IV/C IV is compared with the average of the random realizations (dashed line) for all the systems and also for those above and below  $z = 3$ . Si IV/C IV is clearly seen to be much stronger above  $z = 3$ . Figure 16 shows median Si IV/C IV values as a function of redshift, with errors derived from the distribution of medians in the blank-field realizations. The data again require a rapid jump at around  $z = 3$ , with values of  $0.035 \pm 0.005$  below  $z = 3$  and  $0.10 \pm 0.01$  above.

#### 4. IONIZATION RATIOS

##### 4.1. Introduction

The local shape of the ionizing flux and the value of the ionization parameter may be estimated from the relative distribution of the ionization levels of the various species. Most work to date has concentrated on using Si IV/C IV versus C II/C IV, which, as we have discussed in § 1, is a powerful discriminant of the ionization parameter and of the strength of any break near the He<sup>+</sup> edge. This diagnostic also relies on absorption lines that can be measured outside the forest. The Si IV/C IV versus C II/C IV method is reconsidered (§ 4.2) in the light of the present larger data set. However, the optical depth ratio method developed in § 3.3 provides a powerful way to measure the average abundances of a number of other species (Si III, C III, N V, and O VI) that lie primarily within the Ly $\alpha$  forest. We use this technique in § 4.3 to determine the ensemble properties of these ions as a function of redshift and to show that they can be fitted into a consistent interpretation of the evolution of the shape of the metagalactic flux.

##### 4.2. Si IV/C IV versus C II/C IV

Si IV/C IV versus C II/C IV is shown in Figure 17 for the 29 complexes with  $10^{13} \text{ cm}^{-2} < N(\text{C IV}) < 10^{14} \text{ cm}^{-2}$  and for which the C II line lies longward of the Ly $\alpha$  forest. Open squares denote systems with  $z > 3$  and filled squares those with  $z < 3$ , while downward- and/or leftward-pointing triangles correspond to systems in which Si IV or C II is not detected, with the point positioned at the  $1\sigma$  level. The lines show a range of models computed with the CLOUDY code (Ferland 1993) for a power-law ionizing spectrum with a range of breaks at the He<sup>+</sup> edge at 4 ryd, and with  $\log(\text{Si}/\text{C}) = -0.66$ , typical of metal-poor systems. As was found

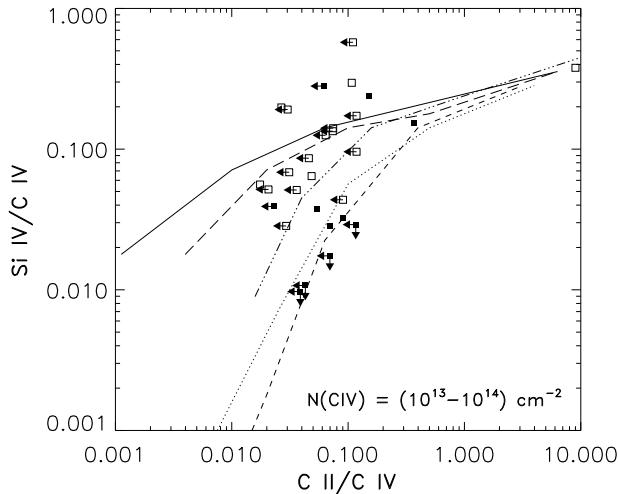


FIG. 17.—Si IV/C IV vs. C II/C IV for complexes with  $10^{13} \text{ cm}^{-2} < N(\text{C IV}) < 10^{14} \text{ cm}^{-2}$  and with C II longward of the forest for systems with  $z < 3$  (filled squares) and  $z > 3$  (open squares). Triangles mark systems in which Si IV or C II is not detected, with the square positioned at the  $1 \sigma$  level. The lines are models computed with the CLOUDY code (Ferland 1993) with  $\log(\text{Si/C}) = -0.66$  for a  $-1.5$  power-law ionizing spectrum (dashed line) and with the addition of a break at the  $\text{He}^+$  edge at 4 ryd of a factor of 2 (dotted line), 10 (dash-dotted line), 100 (long-dashed line), and 1000 (solid line).

previously in SC, while many of the low-redshift systems are consistent with photoionization by a pure power law, most of the high-redshift systems have Si IV/C IV values that are much too high relative to C II/C IV for this to be the case. They are consistent with photoionization by heavily broken power laws with breaks across the  $\text{He}^+$  edge in excess of 20 and softness ratios,  $S \equiv f_{\nu}(4 \text{ ryd})/f_{\nu}(1 \text{ ryd})$ , in excess of 300.

The models of SC were computed with simple broken power laws, and a more extensive discussion of more general spectra may be found in Giroux & Shull (1997). However, Figure 18 illustrates that the general behavior is fairly model-invariant; it compares the data with a wide range of power laws ( $-1.5$  to  $-2.5$ ) again computed with  $\log(\text{Si/C}) = -0.66$ . Unless Si/C is made unreasonably high

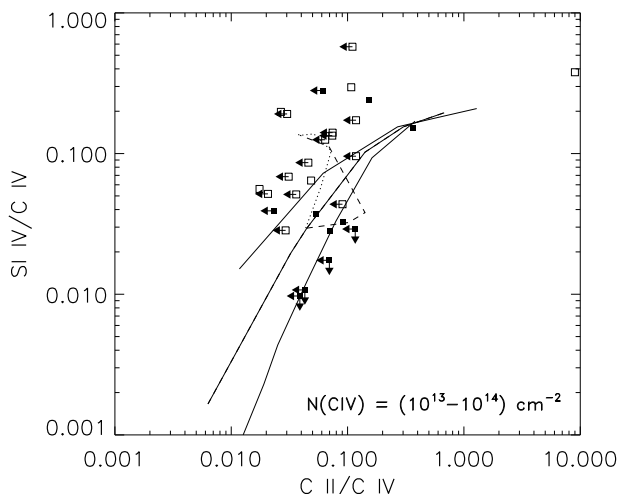


FIG. 18.—Si IV/C IV vs. C II/C IV for the data of Fig. 17 (filled, open squares). The solid lines are CLOUDY models with power-law spectra with index  $-1.5$  (bottom),  $-2.0$  (middle), and  $-2.5$  (top), computed with  $\log(\text{Si/C}) = -0.66$ . The dashed and dotted lines show the effect of the introduction of a break in the spectrum at the  $\text{He}^+$  edge. See text (§ 4.2) for details.

at  $z > 3$ , not even the softest power-law spectrum (*top solid line*) can approach the high Si IV/C IV values. The introduction of the break at 4 ryd moves the lines to a new asymptote, as is illustrated by the dashed and dotted lines. Both are computed with an ionization parameter of  $-1.6$  and a  $-2$  power-law spectrum below 4 ryd, but with a range of break strengths. The dotted line corresponds to the same models as in Figure 17 in which the spectrum above the break is extrapolated with the same spectral index as it has below the break but at the lower flux level, as might be the case if there was a substantial galaxy contribution to the ionizing spectrum. The dashed line is computed instead with a model in which the break is a  $\text{He}^+$  opacity whose cross section reduces as  $E^{-2.7}$  at higher energies. This latter model asymptotes to the same Si IV/C IV values but requires a larger softness ratio of greater than about 2000 to achieve this. It is this effect that gave rise to Rauch et al.'s (1997) incorrect conclusion that  $\text{He}^+$  breaks could not account for the high values of Si IV/C IV in high-ionization systems since they used a recovering spectrum and an intermediate softness parameter (a flux reduction of 100 at 4 ryd). However, as the break becomes large, both models reach the same limiting values, which are consistent with the observed high values of Si IV/C IV and low values of C II/C IV.

In this asymptotic limit of a large break at the  $\text{He}^+$  edge, the Si IV/C IV-to-C II/C IV ratio approaches a single track characterized essentially uniquely by the ionization parameters, which determines, modulo a very weak dependence on spectral index, the C II/C IV value. Therefore most of both the high- and low-redshift systems are consistent with a relatively small range of ionization parameter,  $\log \Gamma = -1$  to  $-2$ , but the higher redshift systems mostly require the high-energy spectrum to be blocked above 54 eV, whereas at the low redshifts this is not generally the case. It is perhaps important to emphasize that this effect is not observationally subtle, and in Figure 19 we show C IV, Si IV, and C II profiles for a sample of the high-Si IV/C IV systems over the redshift range. For the high-Si IV/C IV systems at low redshift, C II is generally clearly present, but many of the high- $z$  high-Si IV/C IV systems are simply missing C II absorption.

#### 4.3. Other Ion Ratios

The optical depth technique discussed in § 3 can also be used to determine the average properties of other important ions such as C III, Si III, and O VI, whose transitions lie below the wavelength of Ly $\alpha$  and for which individual line strengths cannot be reliably determined because of forest contamination.

As with Si IV, the value of  $\tau(X)\lambda_X F_X/\tau(\text{C IV})\lambda_{\text{C IV}} f_{\text{C IV}}$  was determined for the ion, X, at all positions at which significant C IV absorption was present [again,  $\tau(\text{C IV } \lambda 1550) > 0.05$ ], and a distribution of this quantity was constructed. A large number of random realizations were then made in which the C IV redshift was slightly displaced, to determine the backgrounds and errors. Because of forest contamination, which acts as an effective noise source, the errors are larger than for species that lie outside the forest, such as Si IV.

Figure 20 shows the distributions of C III/C IV, N V/C IV, and O VI/C IV for all the available systems and separately for  $z > 3$  and  $z < 3$  systems where the division is possible. The median and mean values and their  $1 \sigma$  errors for a range of ions are given in Tables 3 and 4, respectively. As

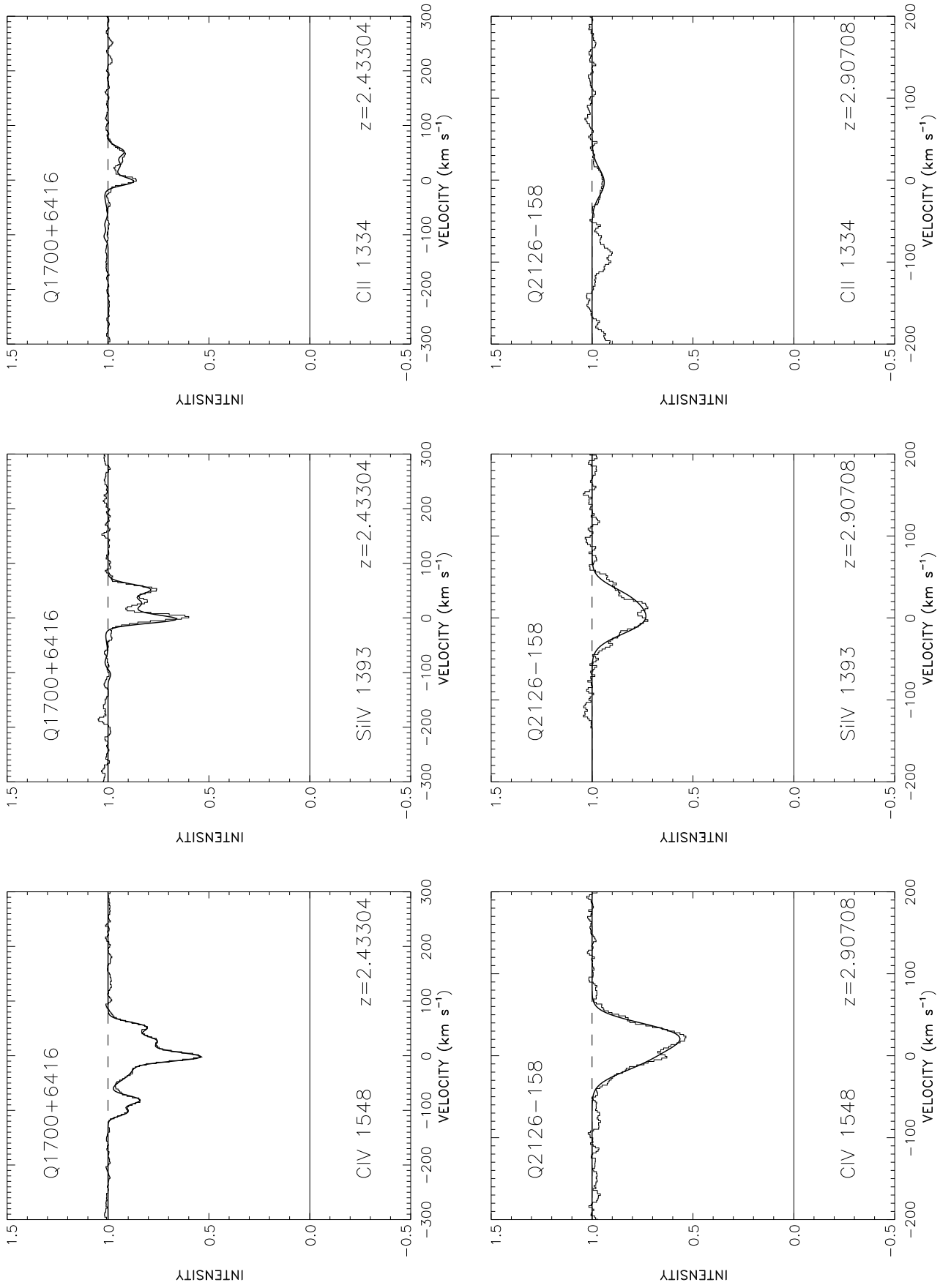


FIG. 19a

FIG. 19.—(a) Sample CIV, SiIV, and CII profiles for systems with a high value of SiIV/CIV at  $z < 3$ , illustrating the absence of CII in these high-redshift systems.

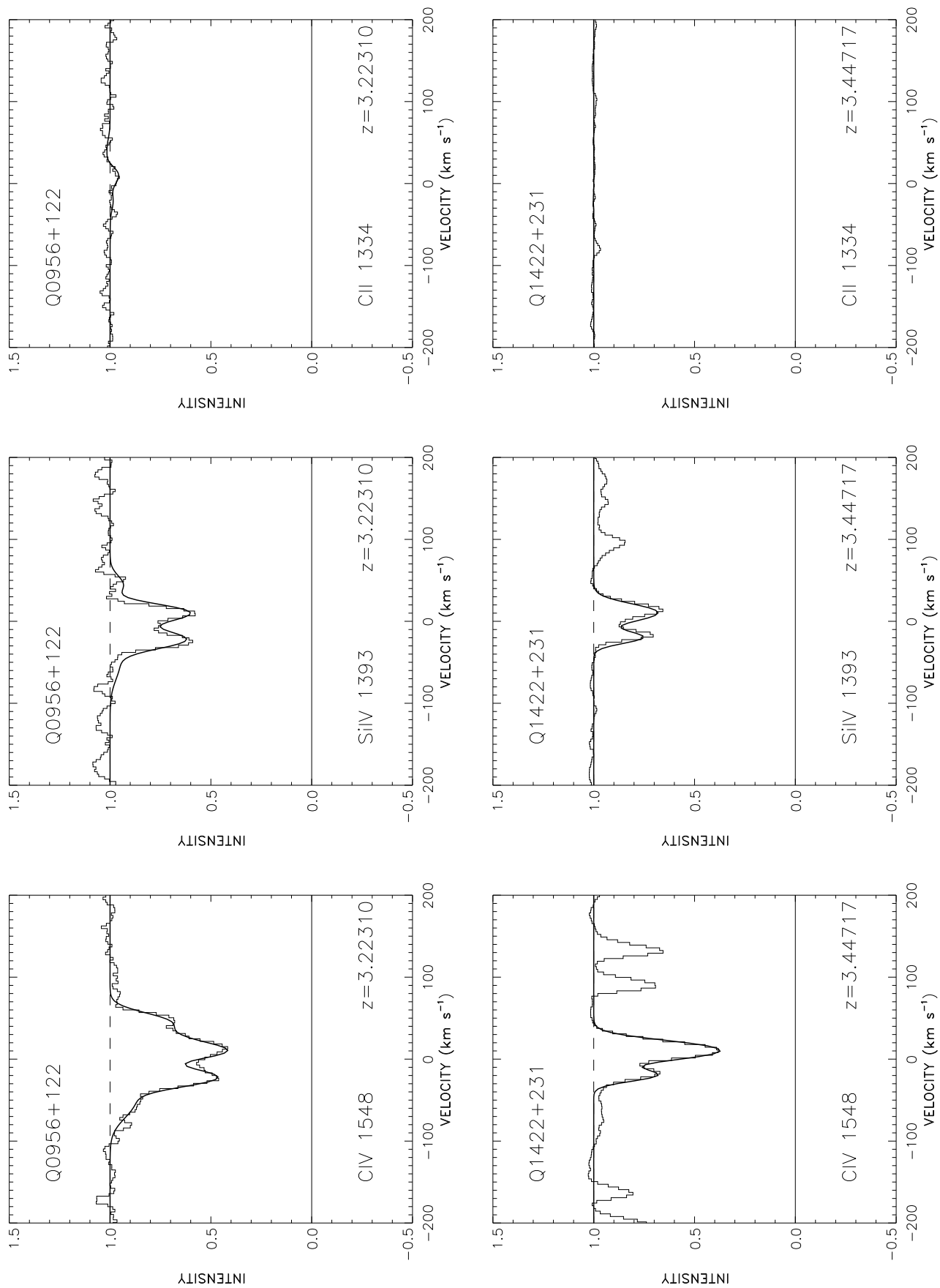


FIG. 19b

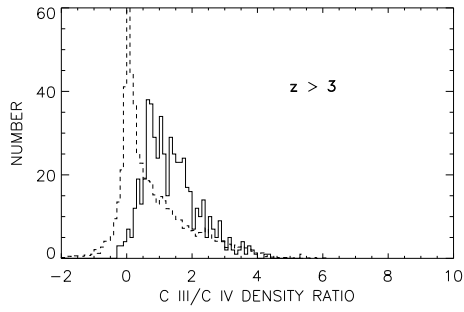


FIG. 20a

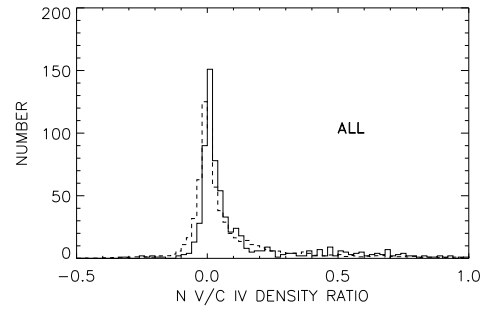


FIG. 20b

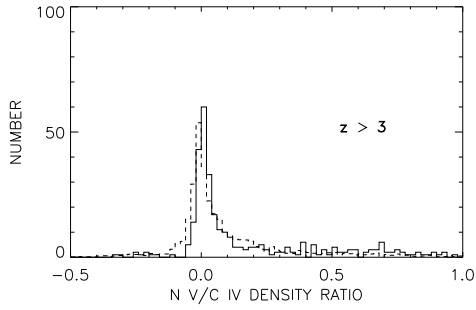


FIG. 20c

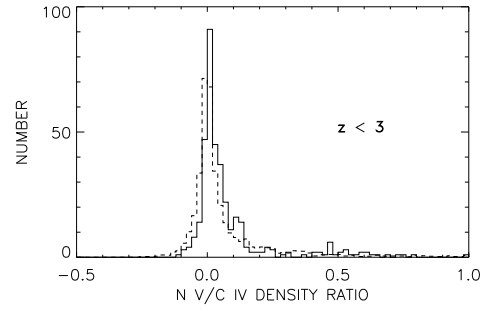


FIG. 20d

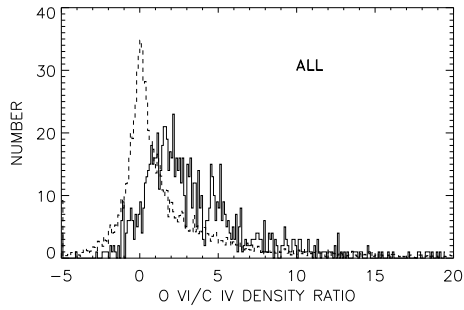


FIG. 20e

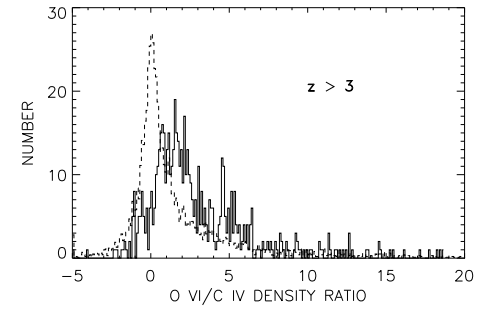


FIG. 20f

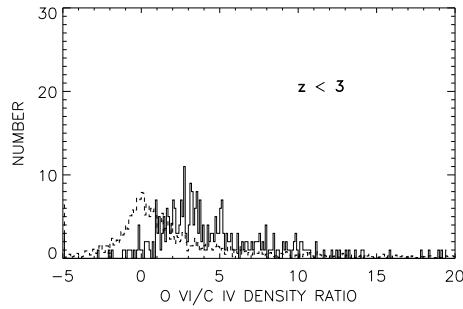


FIG. 20g

FIG. 20.—Distributions of C III/C IV, NV/C IV, and O VI/C IV computed from the optical depth ratios for  $\tau(\text{C IV}) > 0.05$  (solid lines), as in Fig. 15, compared with average blank realizations (dashed lines). Where possible, distributions are also shown separately for  $z > 3$  and  $z < 3$ . Median and mean values and  $1\sigma$  errors are given in Tables 3 and 4, respectively.

TABLE 3

MEDIANS OF COLUMN DENSITY RATIOS WITH RESPECT TO C IV

Ion	All	$z > 3$	$z < 3$
C II.....	$0.02 \pm 0.03$	$0.01 \pm 0.04$	$0.03 \pm 0.09$
C III.....	...	$0.75 \pm 0.25$	...
C IV.....	1	1	1
Si II.....	$-0.001 \pm 0.004$	$0.004 \pm 0.010$	$-0.004 \pm 0.006$
S III.....	$0.029 \pm 0.010$	$0.08 \pm 0.037$	$0.013 \pm 0.019$
Si IV.....	$0.056 \pm 0.003$	$0.10 \pm 0.005$	$0.035 \pm 0.004$
N V.....	$0.019 \pm 0.008$	$0.018 \pm 0.024$	$0.019 \pm 0.006$
O VI.....	$1.97 \pm 0.28$	$1.59 \pm 0.21$	$2.75 \pm 0.78$

TABLE 4

MEANS OF COLUMN DENSITY RATIOS  
WITH RESPECT TO C IV

Ion	All	$z > 3$	$z < 3$
C II.....	-0.28	-0.03	-0.47
C III.....	...	1.97	...
C IV.....	1	1	1
Si II.....	0.08	0.27	-0.07
Si III.....	0.0	0.07	-0.04
Si IV.....	0.12	0.17	0.07
N V.....	0.05	0.09	0.02
O VI.....	1.8	1.3	2.2

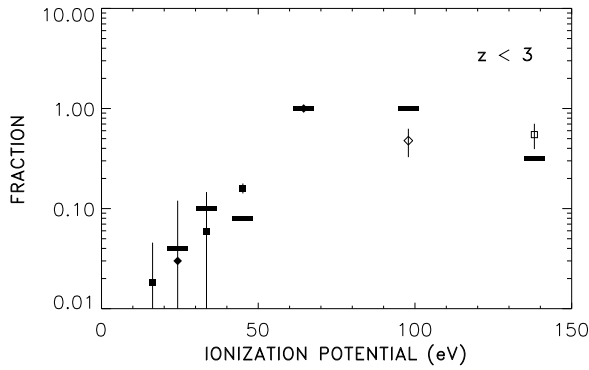


FIG. 21a

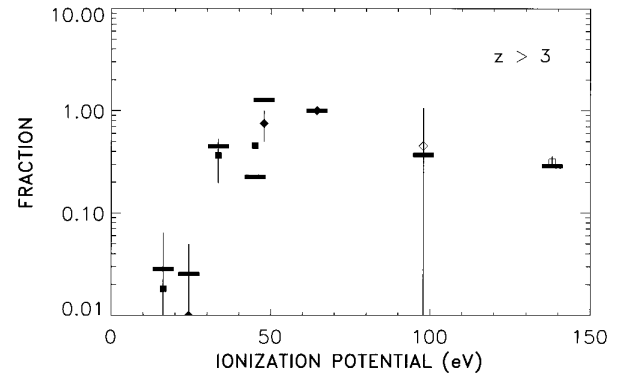


FIG. 21b

FIG. 21.—(a) Quantity  $A_C N(X)/A_X N(C\text{ IV})$  for  $z < 3$  for the ions, X, of Table 3, where  $A_X/A_C$  is the abundance of element X with respect to C, as a function of the ionization potential of the ion, in electron volts. Errors are  $\pm 1\sigma$ . The solid bars show a model in which the ionizing spectrum is a  $-1.8$  power law with  $\Gamma = -1.6$ . (b) Same as (a), but for  $z > 3$ . See text (§ 4.3) for a description of the comparison model (solid bars).

is expected, O VI is strongly detected, with a median  $N(\text{O VI})/N(\text{C IV}) = 1.97 \pm 0.28$ . C III, Si III, and N V are more weakly detected, with a median  $N(\text{C III})/N(\text{C IV}) = 0.75 \pm 0.25$ . Neither Si II nor C II is significantly detected.

The ionization patterns above and below  $z = 3$  are summarized in Figure 21, which uses the more robust median values. The points show the quantities  $A_C N(X)/A_X N(\text{C IV})$ , where  $A_X/A_C$  is the assumed abundance of the element X with respect to C, which is taken to be  $[\text{O}/\text{C}] = 0.5$ ,  $[\text{Si}/\text{C}] = 0.4$ , and  $[\text{N}/\text{C}] = -0.7$ , characteristic of low-metallicity systems. This quantity is plotted against the ionization potential of the ion.

The primary difference between  $z < 3$  and  $z > 3$  remains the much higher abundance of Si IV at the higher redshift. The fractions of the high ions such as N V and O VI are marginally larger at  $z < 3$  than at  $z > 3$ , but the effect is not large. The  $z < 3$  ionization distribution can be reproduced quite well by a very simple model in which the ionizing spectrum is a  $-1.8$  power law and  $\Gamma = -1.6$ ; this is shown as the solid bars in Figure 21a. This highly oversimplified model is, of course, only a rough representation of the ensemble average of conditions in the IGM. However, for  $z > 3$  we need a mix of conditions. As is discussed above, most of the systems must lie in the regions exposed to highly broken spectra in order to reproduce the lower ion ratios, particularly Si IV/C IV, but some fraction of the volume must still be ionized by spectra containing higher energy photons to reproduce the observed O VI, if this is assumed to be produced by photoionization. A model in which 70% of the systems are irradiated by a fully broken spectrum with  $\alpha = -1.8$  below the break and  $\Gamma = -1.5$  and in which 30% of the volume is occupied by a pure  $\alpha = -1.8$  spec-

trum with  $\Gamma = -1.0$  provides a reasonable representation, as is shown by the bars in Figure 21b.

## 5. CONCLUSIONS

I summarize the results of this paper by noting that, irrespective of the analytical methodology adopted, there is a significant change in the ionization balance of forest metal lines that occurs just below a redshift of 3. At lower redshifts, the ionization balance in the forest lines is fully consistent with a pure power-law ionization spectrum with an index of  $-1.8$ , but at higher redshifts the high values of Si IV/C IV seen in most of the forest clouds despite generally low C II/C IV values implies that the ionizing flux must be very soft, with a large break at the He<sup>+</sup> edge. The change occurs quite rapidly between  $z = 2.9$  and  $z = 3$ , just above the redshift at which highly patchy He II Ly $\alpha$  absorption is seen in the quasar HE 2347–4342 (Reimers et al. 1997). The simplest explanation seems to be that we are seeing the redshift at which He II ionizes completely to He III as the He III Strömgren spheres overlap.

I am grateful to the many people at the Keck Telescopes who assisted with these observations and most particularly to Steve Vogt, whose HIRES spectrograph made them possible. I would also like to thank Len Cowie and Esther Hu for obtaining some of the observations on which this work is based, Dieter Reimers for computing positions and magnitudes for unpublished bright quasars, and Sandra Savaglio for providing updated information on higher redshift Si IV/C IV values. The research was supported by the National Science Foundation under grant AST 96-17216.

## REFERENCES

- Boksenberg, A. 1998, Structure and Evolution of the IGM from QSO Absorption Line Systems, ed. P. Petitjean & S. Charlot (Paris: Ed. Frontières), 85  
 Davidsen, A. F., Kriss, G. A., & Zheng, W. 1996, *Nature*, 380, 47  
 Ferland, G. 1993, HAZY, a Brief Introduction to Cloudy (Univ. Kentucky Dept. Phys. Astron. Internal Rep.)  
 Giroux, M. L., & Shull, J. M. 1997, *AJ*, 113, 1505  
 Haardt, F., & Madau, P. 1996, *ApJ*, 461, 20  
 Hogan, C. J., Anderson, S. F., & Rugers, M. H. 1997, *ApJ*, 113, 1495  
 Jakobsen, P., et al. 1994, *Nature* 370, 35  
 Madau, P., & Meiksin, A. 1994, *ApJ*, 433, L53  
 Miralda-Escudé, J., & Rees, M. J. 1993, *MNRAS*, 260, 617  
 Rauch, M., Haehnelt, M. G., & Steinmetz, M. 1997, *ApJ*, 481, 601  
 Reimers, D., Köhler, S., Wisotzki, L., Groote, D., Rodríguez-Pascual, P., & Wamsteker, W. 1997, *A&A*, 327, 890  
 Savaglio, S., Cristiani, S., D'Odorico, S., Fontana, A., Giallongo, E., & Molaro, P. 1997, *A&A*, 318, 347  
 Songaila, A., & Cowie, L. L. 1996, *AJ*, 112, 335 (SC)  
 Songaila, A., Hu, E. M., & Cowie, L. L. 1995, *Nature* 375, 124  
 Zheng, W., Davidsen, A. F., & Kriss, G. A. 1998, *AJ*, 115, 391